Akker et al. *Swiss Journal of Geosciences* (2023) 116:8
https://doi.org/10.1186/s00015-023-00438-z

SGG SGS sc | nat
Swiss Journal of Geosciences

ORIGINAL PAPER

Open Access

Microstructural characterization of natural fractures and faults in the Opalinus Clay: insights from a deep drilling campaign across central northern Switzerland

Ismay Vénice Akker[1,2*], Raphael Schneeberger[3], Marco Herwegh[1], Nathan Looser[5], Lukas Aschwanden[1], Martin Mazurek[1], Kurt Decker[6], Andreas Ebert[7], Marcel Guillong[5], Stefano M. Bernasconi[5], Christoph Schrank[8], Michael W. M. Jones[8], Andrew Langendam[9] and Herfried Madritsch[3,4]

Abstract

The Middle-Jurassic Opalinus Clay is the foreseen host rock for radioactive waste disposal in central northern Switzerland. An extensive drilling campaign aiming to characterize the argillaceous formation resulted in a comprehensive drill core data set. The rheologically weak Opalinus Clay is only mildly deformed compared to the over- and underlying rock units but shows a variety of natural fractures. While these structures are hydraulically indistinguishable from macroscopically non-deformed Opalinus Clay today, their analysis allows for a better understanding of the deformation behaviour in the geological past. Here, we present an overview of the different fracture and fault types recorded in the Opalinus Clay and a detailed microstructural characterization of veins—natural dilational fractures healed by secondary calcite and celestite mineralizations. Macroscopic drill core analysis revealed five different natural fracture types that encompass tension gashes of various orientations with respect to bedding and small-scale faults with displacements typically not exceeding the drill core diameter. The occurrence of different fault types generally fits well with the local tectonic setting of the different drilling sites and with respect to the neighbouring regional fault zones. The microstructural investigations of the various vein types revealed their often polyphase character. Fibrous bedding-parallel veins of presumable early age were found to be overprinted by secondary slickenfibres. The polyphase nature of fibrous bedding parallel veins and slickenfibres is supported by differing elemental compositions, pointing towards repeated fracturing and mineralization events. Direct dating of vein calcites with U–Pb was unsuccessful. Nevertheless, age constraints can be inferred from structural orientations and fault slip kinematics. Accordingly, some of the veins already formed during sediment compaction in Mesozoic times, others possibly relate to Early Cenozoic foreland uplift. The youngest veins are most likely related to Late Cenozoic regional tectonic events, such as the Jura fold-and-thrust belt to the south and the Hegau-Lake Constance Graben to the northeast of the study area. During these latest tectonic events, previously formed veins acted as rheologically stiff discontinuities in the otherwise comparably weak Opalinus Clay along which deformation of the rock formation was re-localized.

Keywords Clay formations, Faulting, Fracturing, Radioactive waste disposal, Deformation temperatures, Carbonate clumped isotopes

Editorial handling: Russell Alexander.

*Correspondence:
Ismay Vénice Akker
vakker@erdw.ethz.ch
Full list of author information is available at the end of the article

1 Introduction

Understanding the deformation behaviour of clay formations is of importance for various sub-surface engineering and exploration industries. The sealing capacity of clay formations makes them a potential host rock for toxic waste repositories (e.g., Bock et al., 2010; Bossart et al., 2017; Gautschi, 2017), effective seals for CO_2 storage (e.g., Metz et al., 2005; Song & Zhang, 2013), and geothermal and hydrocarbon reservoirs (e.g., Ferrill et al., 2014; Ingram & Urai, 1999). Concerning fault systems, clay rocks play an additional role in defining their mechanical strength and seismic behaviour (e.g., Ingram & Urai, 1999; Klinkenberg et al., 2009; Siegesmund et al., 2014; Wenning et al., 2021).

Here, we focus on fractures in the Middle-Jurassic Opalinus Clay, the foreseen host rock for radioactive waste disposal in Switzerland (Bossart et al., 2017; Nagra, 2014). The Opalinus Clay is part of the Mesozoic sedimentary sequence of the northwestern Alpine foreland and the northward adjacent western European Platform. It is over hundred meters thick and characterized by a very high clay-mineral content (57 ± 12 wt%; Mazurek, 2017), resulting in a low permeability and high retention capacity (Bossart et al., 2017; Jaeggi et al., 2018). Due to its extremely low hydraulic conductivity ($< 10^{-13}$ m/s; Gautschi (2017)) and small pore sizes (Houben et al., 2013; Keller et al., 2013), internal mass transfer is diffusion-dominated (Gimmi et al., 2007; Mazurek et al., 2011; Wersin et al., 2016, 2018). Therefore, it is inferred that the Opalinus Clay acted as a stable seal for most of its geological history (De Haller et al., 2014). Nevertheless, deformation related to regional tectonic events appears to have locally enabled transient fluid flow and mineralization along fractures and fault networks in the Opalinus Clay (Jaeggi et al., 2018; Mazurek & Haller, 2018; Mazurek et al., 2018; Smeraglia et al., 2020, 2022; Wenning et al., 2021). Microstructural research on natural tectonites in the Opalinus Clay in the Mont Terri underground rock laboratory, has revealed a variety of deformation structures and indications of the presence of fluids during tectonic deformation (Houben et al., 2013, 2014; Keller et al., 2013; Laurich et al., 2014, 2017, 2018; Orellana et al., 2022). To better understand the long-term sealing capacity of the Opalinus Clay, it is important to assess the links between mechanical behaviour, (micro) deformation structures, and mineralization processes.

The study area is located in central northern Switzerland where the Opalinus Clay is buried underneath Middle and Upper Jurassic carbonates and marls and clastic sediments of the Neogene Molasse Basin (Fig. 1). The area is part of the external Alpine foreland and bound by regional deformation zones of Cenozoic age. In the context of the siting process for a radioactive waste repository within the Opalinus Clay of northcentral Switzerland, the Swiss National Cooperative for the Disposal of Radioactive Waste (Nagra) has carried out an extensive drilling campaign, retrieving drill cores of Opalinus Clay (Fig. 1). These cores allow an unprecedented possibility to study natural fractures within an argillaceous rock formation at burial depths between 450 and 930 m (depending on the drill site), i.e., without near surface chemical alteration or exhumation-induced mechanical disintegration. Here, we present results of a microstructural analysis of selected fractures from eight drill cores (BOZ2-1 and BOZ1-1 from the Bözberg locality, BAC1-1 from Bachs, STA3-1 and STA2-1 from Stadel BUL1-1 from Bülach, MAR1-1 from Marthalen and TRU1-1 from Trüllikon; Fig. 1). The focus is on the small-scale geometry of mineralized and non-mineralized minor faults and tension gashes, which represent the dominant deformation structures. Drillcore samples were investigated macroscopically by low and high-resolution optical light microscopy, scanning electron microscopy (SEM) in combination with energy-dispersive X-ray spectroscopy (EDX), cathodoluminescence light microscopy (CL) as well as with Synchrotron X-ray Fluorescence Microscopy (XFM). In addition, U–Pb dating as well as carbon, oxygen, and clumped isotope analyses were performed on calcite microstructures. The resulting data provide a thorough overview of macroscopic and microscopic natural brittle deformation structures in the Opalinus Clay.

2 Geological background

The study area is located at the distal margin of the northern Alpine foreland basin in central northern Switzerland (Fig. 1a). The Opalinus Clay is part of the Mesozoic sedimentary sequence (Fig. 1b) that evolved in a coastal-epicontinental marine environment following the Late Paleozoic Variscan orogeny (Nagra, 2014; Wetzel et al., 2003; Ziegler, 1990). The latter ended with the post-collisional formation of major Permocarboniferous grabens (Madritsch et al., 2018). Sedimentation of the Opalinus Clay, whose drilled thickness in the study area is between 104 and 122 m, was fast and occurred within 2 Ma at most (Wetzel et al., 2003). It is typically divided into four sub-units of varying texture and clay content, which is the highest at its base and is substituted by increased contributions of carbonates and quartz towards its top (Mazurek & Aschwanden 2020; Lauper et al., 2021). Previous authors suggested that deposition was influenced by reactivation of underlying basement faults (Reisdorf & Wetzel, 2018; Wetzel et al., 2003), but within the area of investigation, indications for syn-sedimentary faulting so far remain vague.

After deposition, the Opalinus Clay in central northern Switzerland witnessed a polyphase deformation and

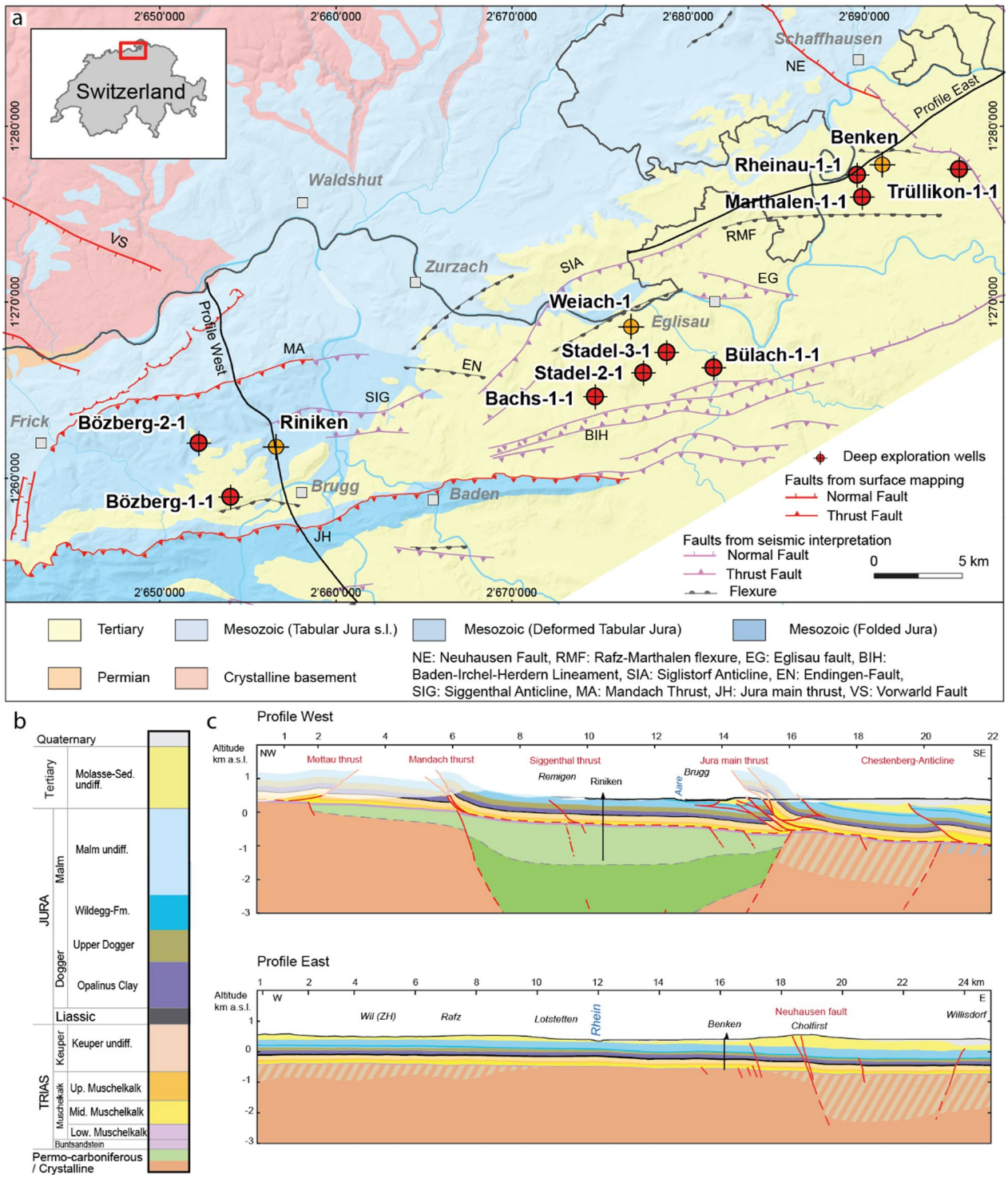

Fig. 1. Geological setting **a** Simplified tectonic map of central northern Switzerland with selected Nagra boreholes (Nagra, 2014). **b** Generic stratigraphic column with the approximately 110 m thick Opalinus Clay. **c** Regional cross sections. Upper section across the Jura fold-and-thrust belt and the lower section orthogonal to the trend of the Hegau-Lake Constance Graben (Jordan et al., 2015)

burial history (Looser, 2022; Madritsch, 2015; Mazurek et al., 2006). Following burial during the Late Jurassic and Early Cretaceous, the region was affected by far-field consequences of the Alpine orogeny, initiating presumably during late Cretaceous times (Pfiffner, 1986; Schmid et al., 1996). Maximum burial depth of about 1700 m and a peak temperature of approximately 85 °C of the top of the Opalinus Clay Formation in the studied area was reached in the Miocene (Mazurek et al., 2006). Uplift and erosion of the Mesozoic sequence during Paleocene to Early Eocene times is thought to result from the formation of an orogenic flexural forebulge (Kempf & Pfiffner, 2004; Sinclair & Allen, 1992). Early Cenozoic erosion estimates vary between 750 and 1050 m (e.g. Mazurek et al., 2006).

Following the formation of the European Cenozoic rift system including the Upper Rhine Graben and the Black Forest and Vosges Massifs to the northwest of the study area in Eocene–Oligocene times (Dèzes et al., 2004; Hinsken et al., 2007), sedimentation re-commenced during Middle to Late Oligocene. During this time, the region became part of the northern Alpine Molasse Basin (Pfiffner, 1986; Sinclair & Allen, 1992; Willett & Schlunegger, 2010) and a sequence of clastic sediments was deposited throughout the Miocene. Contemporaneously, two tectonic realms evolved, which resulted in today's structural setting of the study area: in the northeast, south of Schaffhausen, roughly NE-SW directed extensional to transtensional deformation resulted in the formation of the Hegau-Lake Constance Graben, starting around the Early Miocene (Burdigalian; Hofmann et al., 2000; Schreiner, 1992). The graben is associated with NW–SE striking normal faults, inherited from pre-existing Variscan basement structures (Egli et al., 2017). Seismotectonic data suggest that this deformation is still ongoing (Diehl et al., 2023). The NW–SE trending Neuhausen Fault, studied in detail based on 3D seismic data (Birkhäuser et al., 2001; Roche et al., 2020), is the westernmost of these faults (Fig. 1a, c). Initiating at ~ 14.5 Ma at the latest and lasting until at least ~ 4.5 Ma (Looser et al., 2021; Smeraglia et al., 2021), foreland contraction and the formation of the Jura fold-and-thrust belt took place related to nappe stacking in the Central Alps (distant push; e.g., Laubscher, 1961). The basal décollement of this thrust belt is located in Middle to Upper Triassic evaporites (Jordan, 1992; Sommaruga, 1999; Sommaruga et al., 2017). However, at least in the strongly deformed parts of the central Jura fold-and-thrust belt, the Opalinus Clay has presumably acted as secondary detachment during thrusting (Nussbaum et al., 2018; Schori et al., 2015) and as a hydrogeological barrier during syn-tectonic fluid flow (Smeraglia et al., 2022). As our study area is located at the easternmost tip of the Jura fold-and-thrust belt, just north of the so-called "Jura Main Thrust" which constitutes the Lägern Anticline (Fig. 1a, c), the amount of shortening in this area decreases from approximately six to zero km from west to east (Jordan et al., 2015; Malz et al., 2016). Nevertheless, contractional deformation in the study area reached beyond this main thrust front and further into the foreland, resulting in the formation of isolated thrust faults (e.g., Mandach Fault; MA in Fig. 1a, c; Malz et al., 2020).

3 Methodology

3.1 Macroscopic structural analysis

As part of the deep exploration drilling campaign of Nagra, cores were retrieved from the Opalinus Clay in eight vertical boreholes (BOZ2-1, BOZ1-1, BAC1-1, STA3-1, STA2-1, BUL1-1, MAR1-1, and TRU1-1; for locations see Fig. 1). The cores were oriented towards true North based on the correlation of deformation structures visible on the core and oriented geophysical borehole images. After orientation of the cores, all macroscopically visible deformation structures were recorded including their orientation, extent, mineralization, stretching lineation, and shear sense (Ebert & Decker, 2019).

3.2 Encasing sample cores in epoxy resin and cutting

For the microstructural investigation, we selected a representative set of macroscopic deformation structures (cf. Sect. 4.2.). For protection and stabilization of selected sections, the drill cores (9.4 cm in diameter) were cased in epoxy resin (Sikadur 52 Injektion Normal) and cut into thin section blocks. For this purpose, cylindrical moulds were made by placing a PVC tube (10.4 cm in diameter) around the drill core, and the empty space was filled with epoxy resin. A PVC base plate was used to avoid direct contact between PVC and core, and wooden sticks were placed as spacers between base plate and core as well as around the core walls. To speed-up polymerization, we used a heating plate at a maximum temperature of 35 °C. Finally, the mould was removed after cutting through its long axis and the core was cut into blocks from which thin sections were made. For dry and heat free cutting, we used a mitre saw with diamond blade. All cuts were subsequently coated again with resin and dried before any further cutting. Thin sections (thickness of 30 µm) were made using oil instead of water to avoid disintegration of the sample material. In case a lineation direction was observed, the thin section block was cut parallel to this lineation. See Additional file 1: Fig. S1 for a general overview of how all thin section blocks were cut and how the orientation of the structures in the photomicrographs can be retrieved. In this manuscript all photomicrographs of thin sections are marked by a white arrow indicating the downhole direction.

3.3 Microstructural imaging

In a first step, the microstructures were investigated under transmitted light at thin-section scale using a Zeiss Axioplan petrographic microscope equipped with an automatic stage. In a second step, regions of interest were analyzed in detail with scanning electron (SEM) and cathodoluminescence light (CL) microscopy at sub-mm scale. SEM analyses were conducted using a Zeiss EVO 50 SEM equipped with backscatter and secondary-electron detectors at the Institute of Geological Sciences, University of Bern. CL microscopy was carried out using a CL8200 Mk5-2 Optical Cathodoluminescence System operated at 15 kV acceleration voltage and 250 µA beam current at the Geological Institute, ETH Zürich.

3.4 Quantitative and qualitative geochemical analysis calcite

3.4.1 Energy-dispersive X-ray spectroscopy (EDX) on calcite

Identification of the mineral-chemistry of calcite was done on thin sections using spot analysis on a ZEISS EVO50 SEM in combination with an EDX system. The SEM was operated at 15 kV acceleration voltage, 1.2 nA beam current, and a measurement time of 50 s per spot. For quantification of the variability of Mg and Fe in calcite, we used the "TEAM version: V4.5-Released" software. The data was acquired standard-free using a ZAF (atomic number (Z) effect, absorption (A) effect, and fluorescence excitation (F) effect) correction. All oxide values were recalculated to atoms per formula unit.

3.4.2 Electron microprobe WDS mapping

Wavelength-dispersive spectroscopy (WDS) mapping was performed on a JEOL 8200 superprobe instrument at the Institute of Geological Sciences, University of Bern operated at 15 kV acceleration voltage and 3e-8 A probe current. For the maps with size of 500 × 500 µm, we used a step size in x- and y-direction of 1.75 µm and a dwell time of 150 ms. For data processing, we used XMapTools 4 (Lanari et al., 2014, 2019).

3.4.3 Synchrotron X-ray fluorescence microscopy (XFM)

For the XFM experiment, a thin section (thickness of 30 µm) was mounted on a high-purity fused quartz slide (50.8 × 25.4 mm) without cover slip (Schrank et al., 2021) and mapped at the XFM beamline of the ANSTO Australian Synchrotron (Howard et al., 2020) on a standard sample mount. A region of interest containing fibrous veins and slickenfibres (9.628 mm × 5.302 mm) was scanned with a dwell time of 1 ms and a pixel size of 2 µm with an 18.5 keV X-ray beam focused to a ~ 2 µm spot at the sample, using a Kirkpatrick-Baez mirror pair. The total scan time amounted to 214 min. Excited X-ray fluorescence photons were recorded in event mode with the Maia (Rev D) detector system (Ryan et al., 2018; Siddons et al., 2014) in its usual backscatter geometry. The Dynamic Analysis method (Ryan & Jamieson, 1993) implemented in GeoPIXE (Ryan et al., 2005) was used for spectral deconvolution. Calibration with metallic foils of known composition yielded quantitative concentration maps from K to Zr.

3.5 U–Pb dating of secondary calcite

U–Pb laser ablation inductively coupled plasma mass spectrometry (LA-ICP-MS) analyses were conducted at ETH Zürich using an ASI RESOlution S-155, excimer (ArF, 193 nm) laser ablation system coupled to a Thermo Element XR sector-field ICP-MS on polished thick sections (thickness of 100 µm). The analytical and data reduction procedures follow Roberts et al. (2017) using NIST SRM614 and WC-1 calcite as primary reference materials and Guillong et al. (2020) using spot sizes of 110 and 163 µm and pulse rates of 5 and 7.4 Hz, respectively, ensuring a constant aspect ratio of the ablation craters. U–Pb dates were calculated from Tera-Wasserburg concordia lower intercepts using the IsoplotR software package (Vermeesch, 2018), and a long-term excess variance of 2% relative was propagated by quadratic addition to the uncertainty of the individual lower intercept dates (Guillong et al., 2020). The secondary reference materials ASH-15D (Nuriel et al., 2021), JT (Guillong et al., 2020), and an additional in-house reference material (PDF-9B) were analyzed for validation (Additional file 1: Fig. S8). Correction for matrix effects with WC-1 was done with anchoring the $^{207}Pb/^{206}Pb$ initial-lead ratio to 0.85, while samples and secondary reference materials were not anchored. No disequilibrium correction was applied. All uncertainties are reported at the 95% confidence level. Prior to and after LA-ICP-MS measurements, the samples were analyzed by cathodoluminescence light microscopy to identify growth zonings and to detect misplaced ablation spots which were then excluded from the data.

3.6 Clumped isotopes

Clumped isotope measurements were conducted on 1–2 mg of calcite powder per sample at ETH Zurich using a Thermo Scientific Kiel IV carbonate device coupled to a Thermo Scientific MAT253 or a MAT253 Plus isotope ratio mass spectrometer (IRMS) based on the methods described by Meckler et al. (2014) and Müller et al. (2017). In addition to the removal of water and noncondensable gases by the Kiel IV carbonate device, potential isobaric contaminations were removed by a Porapak Q resin held at − 40 °C. Backgrounds on m/z 44–47 were determined at the beginning of each analytical session by high-voltage peak scans at five different intensities between 10 and 30 V (Bernasconi et al.,

2013). Data reduction was carried out with the Easotope software package (John & Bowen, 2016). Oxygen and carbon isotope ratios are reported relative to VPDB and are within analytical uncertainty of ± 0.10 ‰ for $\delta^{13}C$ and ± 0.20 ‰ for $\delta^{18}O$ (± 1 std. dev). Clumped isotope data are reported in the I-CDES scale (Bernasconi et al., 2021). Δ_{47} temperatures are calculated using the Anderson et al. (2021) calibration and the oxygen isotopic compositions of the precipitating fluids $\delta^{18}O_{fluid}$) are calculated using the calibration of Kim and O'Neil (1997). Measurements failing outlier tests and with a deviation from the median Δ_{47} value of the sample of ≥ 0.070‰ (3% of all measurements) were not considered. Analytical errors in Δ_{47} temperatures are reported at the 95% confidence level (Fernandez et al., 2017).

4 Results

4.1 Macroscopic deformation structures

In general, the Opalinus Clay is macroscopically weakly deformed compared to the more competent units above and below (e.g., the above-lying limestones of the Malm group or the underlying Keuper (cf. Figs. 1 and 2). In fact, the average frequency of fractures within the Opalinus Clay ranges between 0.4 and 1.6 fractures/core meter. The average fracture frequency in the entire drillings over all lithologies ranges between 1.4 and 2.8 fractures/core m. By comparison, in the Bänkerjoch Fm., which is part of the Keuper group, the fracture frequency varies between 3.8 and 7.7 fractures/core m.

4.1.1 Terminology

A full inventory of the encountered macroscopic structures in the Opalinus Clay per borehole is given in Table 1. We use the term fracture to overarchingly describe any brittle structural discontinuity (Ebert & Decker, 2019). The macroscopic drill core mapping allowed us to distinguish five types of natural fractures (Fig. 3, Table 1).

i) Joints: barren, closed fractures on which no measurable slip is observed at the scale of observation (Hancock 1985).
ii) Tension gashes: extensional fractures showing no macroscopic signs of shear deformation, hence presumably dilatational but featuring secondary mineralization.
iii) Mirror-like fault planes: single fractures with smoothed, polished or shiny surfaces with striation implying shear deformation but typically not featuring secondary mineralization.
iv) Fault planes: single, striated fractures with clear signs of shear failure (Peacock et al., 2016) and most often also featuring secondary mineralization.
v) Fault zone: composite deformation zones with macroscopically recognizable shear component constituted by various natural fractures types, some of them featuring secondary mineralization (tension gashes, mirror-like and mineralized fault planes).

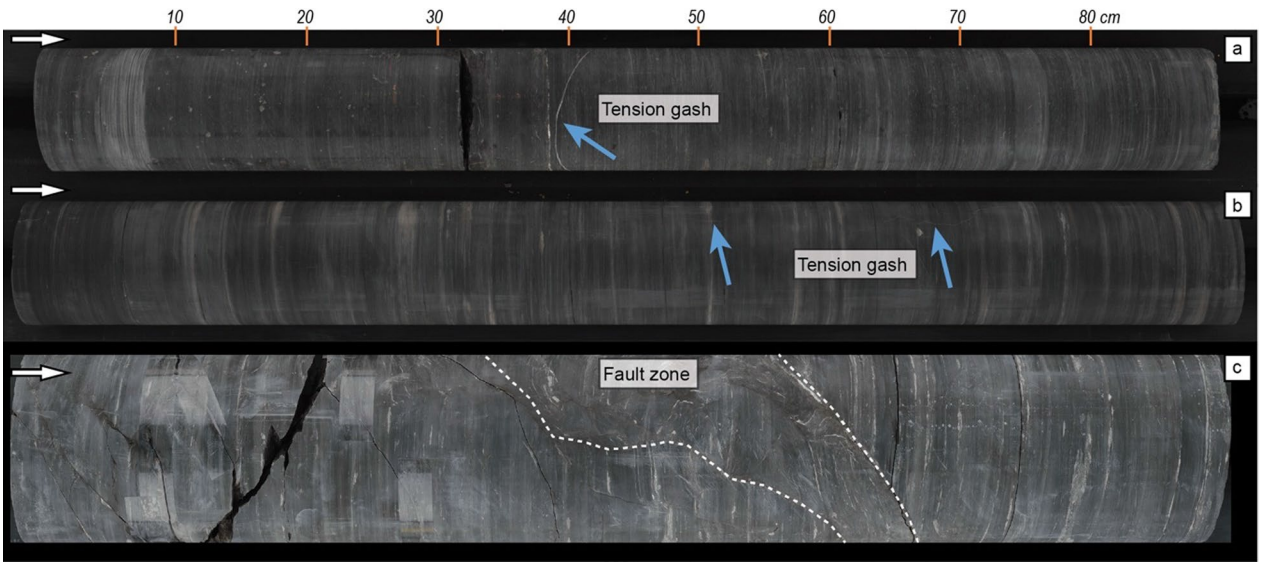

Fig. 2 Three core segments showing the general appearance of the Opalinus Clay and the typically sampled structures (core diameter is 95 mm). **a** This core is from STA2-1 at 821.53–822.45 m MD (core depth). **b** Core from BOZ2-1 at 541.33–542.25 m MD (core depth). **c** Core from BOZ2-1, 510.02 to 510.70 m MD (core depth)

Table 1 Inventory of macroscopic fractures per borehole

	BOZ2-1		BOZ1-1		BAC1-1		STA2-1		STA3-1		BUL1-1		MAR1-1		TRU1-1	
OPA Thickness [m]	**122.14**		**121.11**		**106.57**		**105.53**		**108.68**		**104.15**		**115.05**		**111.49**	
	Number	**%**	**Number**	**%**	**Number**	**%**	**Number**	**%**	**Number**	**%**	**Number**	**%**	**Number**	**%**	**Number**	**%**
J	0	0	0	0	1	1	0	0	0	0	0	0	1	1	0	0
TG	28	14	25	19	42	39	40	51	24	33	1	2	20	12	1	2
MirFP	84	43	62	46	31	29	19	24	11	15	18	40	52	32	45	87
FP	78	40	45	34	32	30	18	23	35	49	24	53	87	53	4	8
FZ	4		1		1		1		2		0		3		2	
UF	0	0	1	1	0	0	0	0	0	0	0	0	1	1	0	0
Count	194		134		107		78		72		45		164		52	
Count / core m	1.6		1.1		1.0		0.7		0.7		0.4		1.4		0.5	
Veins / core m	0.23		0.21		0.39		0.38		0.22		0.01		0.17		0.01	
Shear sense																
Up	57	68	29	76	17	65	6	100	12	55	8	100	5	7	0	0
Down	24	29	6	16	8	31	0	0	10	45	0	0	63	89	19	95
Strike-slip	3	3	3	8	1	4	0	0	0	0	0	0	3	4	1	5
Counts	84		38		26		6		22		8		71		20	

J Joint, *TG* Tension gash, *MirFP* mirror-like fault plane, *FP* fault plane, *FZ* fault zone, *UF* unassigned fracture, *Up* reverse shear sense; *Down* normal shear sense; *Strike slip* strike-slip shear sense. Faults of syn-sedimentary origin were excluded from kinematic analysis

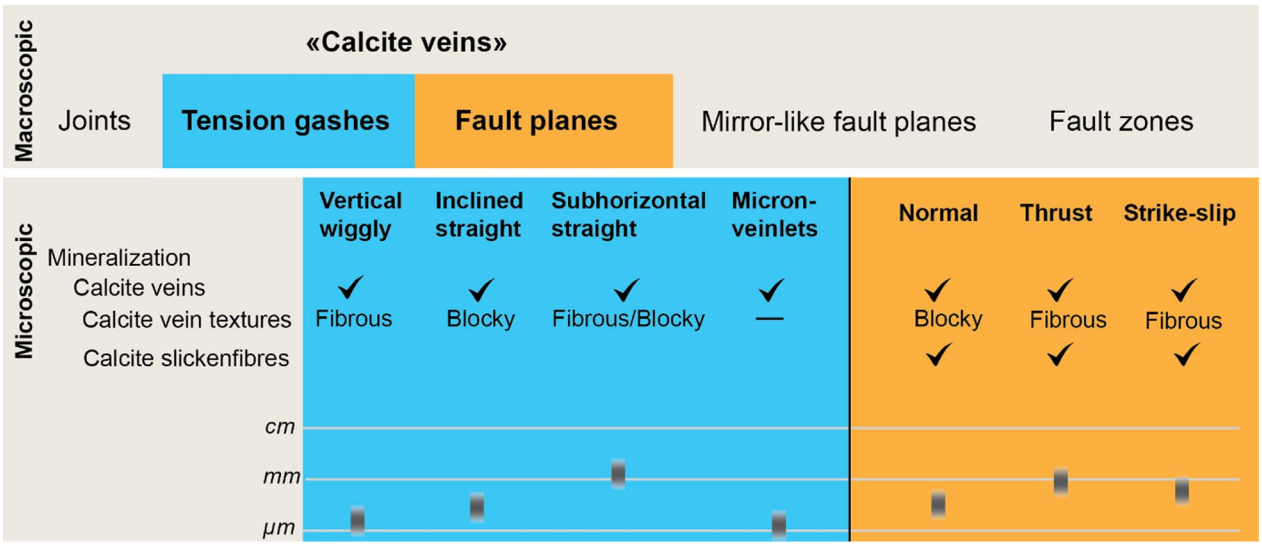

Fig. 3 Overview of analysed structure types. The upper part presents the five types of macroscopically described structures with fault zones representing composite zones constituted by various natural fracture types (see Fig. 4). The lower part shows the types of microscopically analysed "veins" (tension gashes and mineralized fault planes) including the microstructural texture and approximated average vein width

The term "veins" is used here in a phenomenological sense, applied to all types of the above-mentioned fractures that feature secondary mineralization. It is these so-called veins, including apparent tension gashes and fault planes that were targeted for microstructural analysis. The vast majority of veins have thicknesses below 1 mm but occasionally significantly thicker veins were also observed (e.g., in BAC1-1 up to 10 mm or in BOZ2-1 a singular mineralized fault plane with a width up to 15 mm). Further microstructural analysis of veins is outlined in Sect. 4.2.

The remaining fracture types not further analyzed microstructurally are joints, mirror-like fault planes, and fault zones. Joints are only very rarely observed in the

Opalinus Clay (cf. Table 1) and were not further investigated here because they lack any mineralization and therefore are out of the scope of this study. Mirror-like fault planes were also not further analyzed microstructurally because of the requirement for additional preparation techniques (e.g., BIB polishing) to account for their fine-grained nature. Typically, mirror-like fault planes are non-dilative fractures that occur with solely clay minerals that make striated shiny surfaces (Fig. 4a,b). From the few observed fault zones (e.g., Fig. 4d,e) only small selected areas could be investigated. They were found to be constituted by multiple individual fault planes and mirror-like fault planes (Fig. 4d). In addition, calcite veins with blocky textures (Fig. 4e) and dilation/tectonic breccias with dismembered clasts are present in such fault zones.

4.1.2 Fracture distribution across the formation

In all studied drill cores, except for STA2-1, fault planes (including mirror-like fault planes) are the most prominent fracture type (relative abundance 47–94%), followed by tension gashes (relative abundance 2–51%).

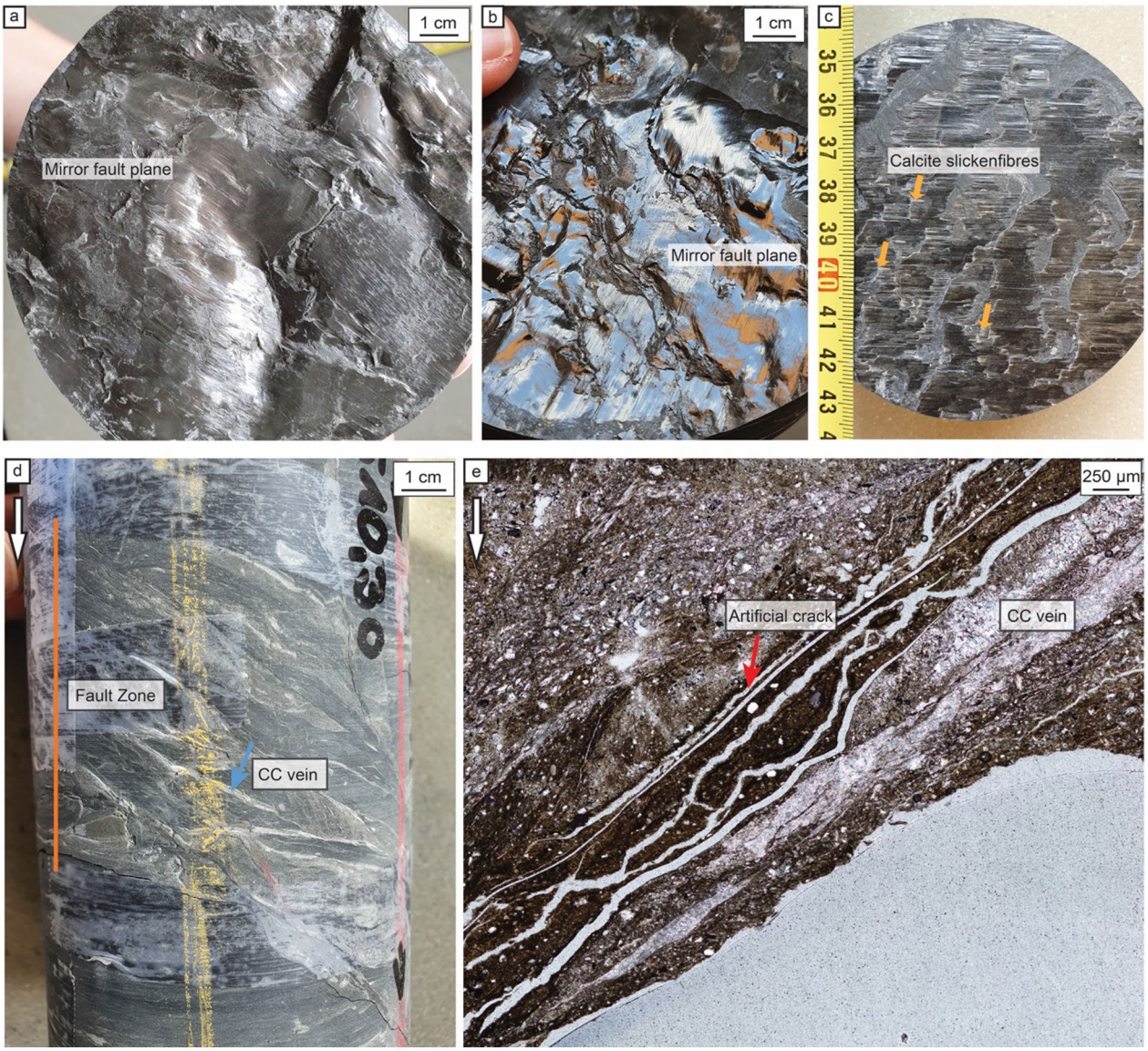

Fig. 4 Macro and microphotographs of mirror fault planes and fault zones. **a**, **b** Mirror-like fault planes with striated clay minerals. **c** Fault plane with striations and calcite slickenfibres. **d** Macroscopic photograph of a core including a several cm-wide fault zone (orange line). **e** Microscopic photograph of cm-scale area in (**d**) showing an individual fault plane within the fault zone. Note that the latter is a composite deformation structure which is also associated with calcite veins and dismembered clasts

By comparison, joints and fault zones are only rarely observed within the Opalinus Clay (cf. Table 1).

In most boreholes (BAC1-1, STA3-1, STA2-1, BUL1-1, MAR1-1 and TRU1-1) these fractures occur clustered, resulting in narrow more strongly fractured zones within the Opalinus Clay and are separated by larger sections practically free of natural fractures (Figs. 2 and 5). Only in the two boreholes in the west of the study area (BOZ1-1 and BOZ2-1) fractures occur more pervasively across the formation (Fig. 5).

4.1.3 Observations on fault-slip kinematics and displacements

Fault planes and mirror-like fault planes pre-dominantly strike from N to E with a dominate strike 70° from N or ENE-WSW (Decker et al., 2022). The predominant sense of shear of the fault planes and mirror-like fault planes varies between the boreholes (Table 1). In boreholes BOZ1-1, BOZ2-1, STA2-1, and BUL1-1, reverse shear senses dominate. In STA3-1, reverse (55%) as well as normal shear senses (45%) were common. In boreholes MAR1-1 and TRU1-1, a dominance of normal shear senses was recorded. The proportion of strike-slip shear sense is low across all boreholes (below 5%). However, this might be due to the well-known underestimation of steep fault planes in a vertical borehole. The dip of normal faults in the cores is on average 25°, of thrust fault planes 14°, and of fault planes with a strike-slip component 53°.

The absence of strain markers at the cm- to mm scale of observation in the relatively homogeneous Opalinus Clay precludes firm statements on typical displacements along slickensides. However, for the majority of the analyzed fault planes, the lengths of syn-kinematic calcite fibres with long axes oriented parallel to the shear direction indicate slip distances of several mm

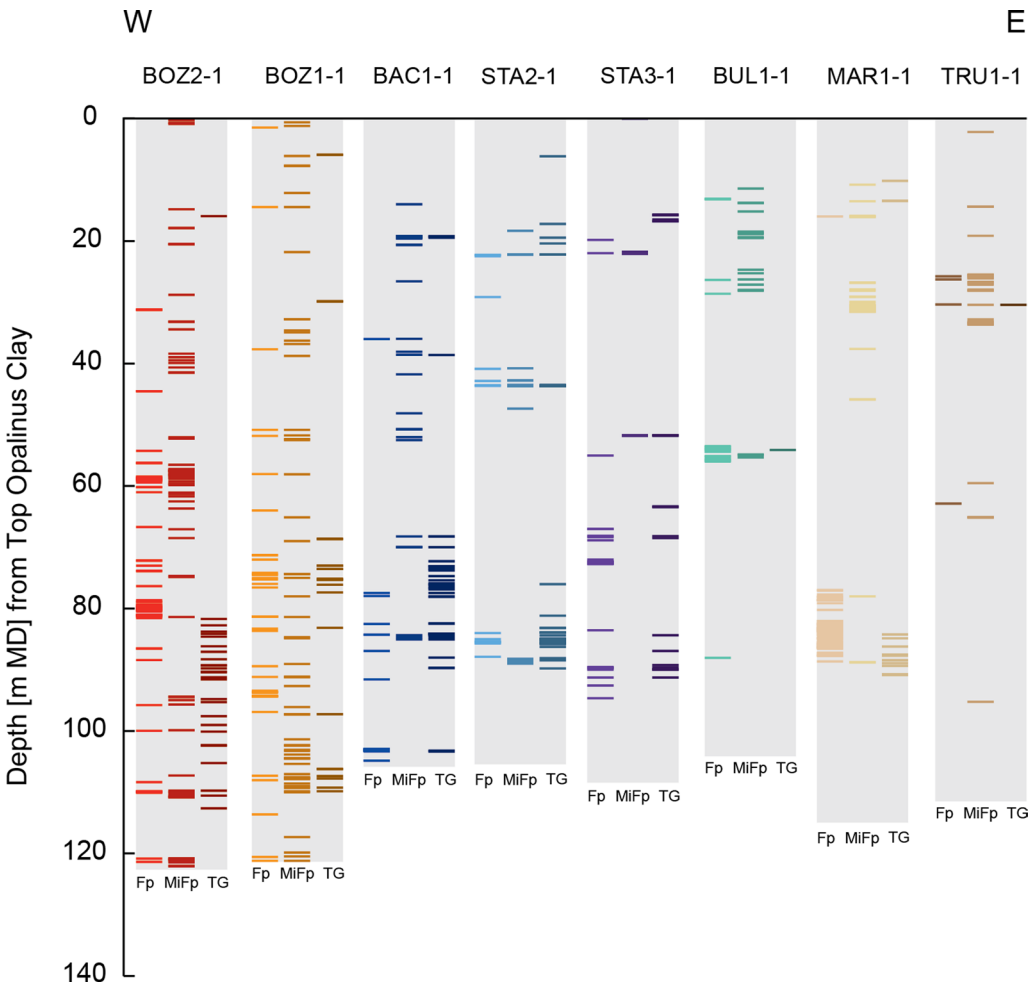

Fig. 5 Spacing analysis of macroscopic natural fractures across the Opalinus Clay in the investigated boreholes. *Fp* fault plane, *MiFp* mirror-like fault plane an *TG* tension gashes

to few cm at most. Mineralized fault zones within the Opalinus Clay, such as in STA2-1, might indicate displacements larger than the core diameter (> 95 mm). Given the '1D' nature of the drill cores, no information about the lateral dimensions of the investigated fractures exists. However, the measured fracture widths allow at least a qualitative discrimination of the fractures in terms of their relative dimensions (Fig. 3).

4.2 Microscopic deformation structures

For microstructural analysis, samples were selected from mineralized fracture types including tension gashes and mineralized fault planes, generally referred to as veins (Fig. 3). These structures were distinguished during macroscopic characterization of the cores and occur in all boreholes. Table 2 and Additional file 1: Fig. S2 provide an overview of presented key samples and an overview with all studied samples can be found in Additional file 1: Table S1.

Microscopic analysis of the veins revealed three types of deformation features at thin-section scale: (1) Dilative tension gashes with different orientations and secondary mineral phases (calcite) showing a variety of textures, (2) faults including normal, strike-slip, and thrust faults with calcite and celestite slickenfibres and (3) micron-veinlets that are consistently found in relation to thrust faulting.

4.2.1 Dilative tension gashes

Dilative tension gashes are predominantly filled with calcite and show different structural orientations and microfabrics. Considering their orientation with respect to the bedding, we distinguish vertical tension gashes with a wiggly shape, oblique tension gashes with straight walls, and sub-horizontal tension gashes with straight walls.

Wiggly-shaped vertical tension gashes typically have widths of about 0.5 mm (Fig. 6a,b). Tension gashes of this type show an internal antithetic fibrous texture, with fibres growing horizontally in two directions from the median line. The median line includes small micron-sized inclusions (e.g., calcite and clay particles). Despite the irregular nature of the vein walls, calcite fibres are straight, undeformed, and bedding-parallel.

Oblique tension gashes with straight vein walls have thicknesses up to ca. 0.5 mm. These tension gashes are often filled with calcite and the fracture planes form angles of 10 to 45° with the bedding. The internal texture of these so-called composite veins shows typical antitaxial crack-seal microfabrics (Fig. 6c,d; Ramsay, 1980; Ramsay et al., 1983). The cores of these tension gashes show

Table 2 Structural measurements of the selected samples

Borehole	Depth [m]	Structure	Fault plane Dip direction [°]	Fault plane Dip [°]	Lineation Azimuth [°]	Lineation Plunge [°]	Shear sense	Interpreted Deformation phase
BOZ1_1	619.65	Strike-slip fault	237	56	155	25	Up/dextral	N-S shortening
BOZ2_1	482.70	Thrust fault	154	30	180	25		NNW-SSE shortening
BOZ2_1	507.70	Thrust fault	305	34	20	20	Up	
BOZ2_1	527.87	Thrust fault	171	12	142	8		NNW-SSE shortening
BOZ2_1	531.77	Thrust fault	155	17	155	15	Up	NNW-SSE shortening
BOZ2_1	541.82	Tension gash—vertical wiggly	236	83	–	–	–	E-W extension
BOZ2_1	546.69	Tension gash—vertical wiggly	207	75	–	–	–	NW–SE extension
STA2_1	793.15	Normal fault	356	15	–	–	–	NW–SE extension
STA3_1	830.87	Tension gash—Inclined straight	77	25	–	–	–	N-S shortening
STA3_1	851.27	Thrust fault	136	5	182	2	Up	NNW-SSE shortening
MAR1_1	668.85	Normal fault	186	31	181	29	Down	–
MAR1_1	676.56	Tension gash	102	7	–	–	–	SSW-NNE or SSE-NNW shortening
MAR1_1	676.56	Normal fault	230	33	–	–	Down	E-W extension
TRU1_1	846.70	Normal fault	96	59	10	15	Sin	–
TRU1_1	849.70B	Normal fault	–	–	–	–	–	–

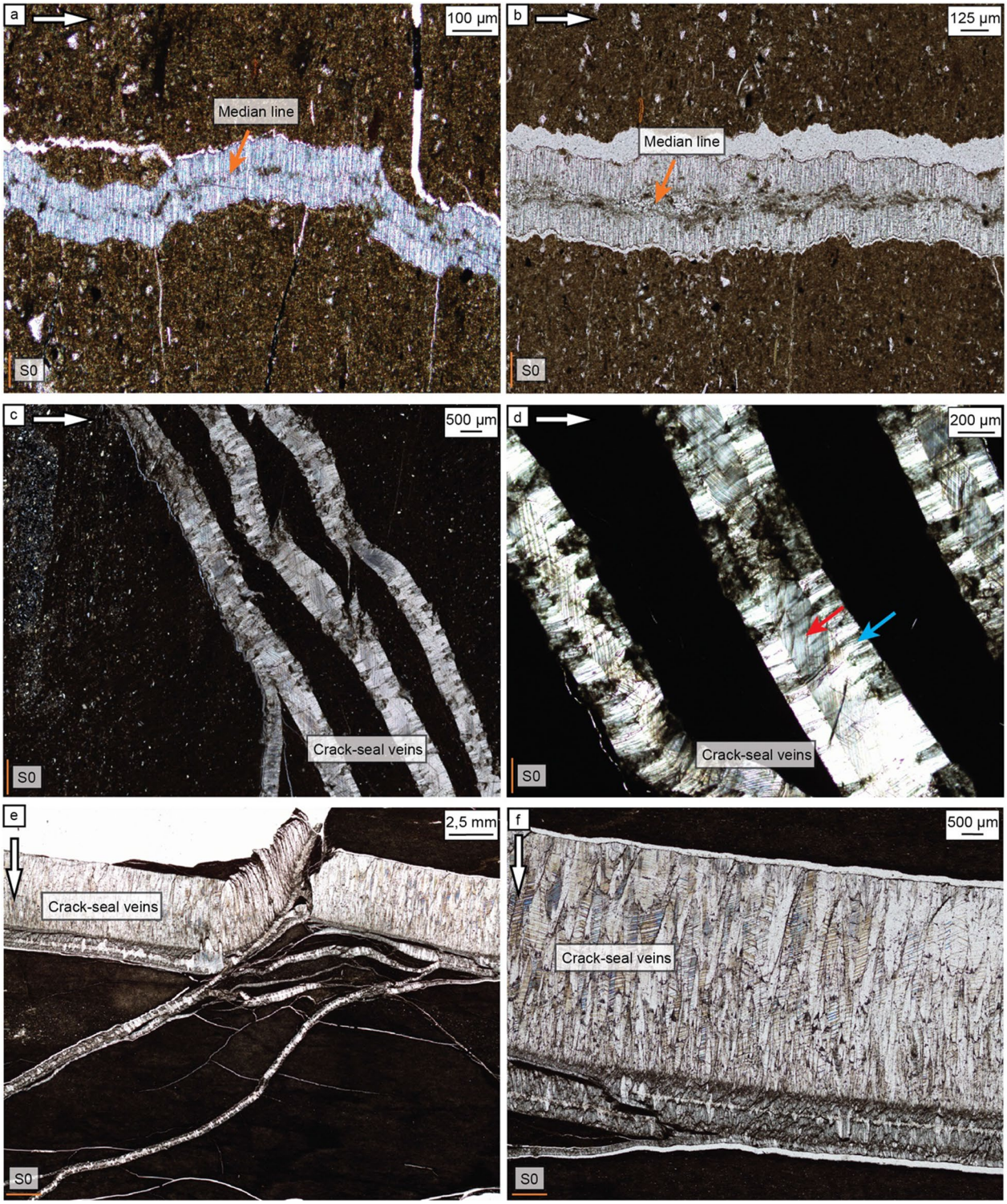

Fig. 6 Overview of microscopic images of three different types of tension gashes filled with calcite ("veins"). **a**, **b** Optical light micrographs of vertical veins with wiggly walls. Calcite fibres are oriented parallel to the bedding (S0) (sample BOZ2_1_541.82 (**a**) and BOZ2_1_546.69 (b)). **c**, **d** Optical light micrographs of a network of oblique veins with straight walls showing elongate-blocky calcite veins with crack-seal microfabrics. The veins cut the bedding (S0) under a 45° high angle (sample STA3_1_830.87). **e**, **f** Optical light micrographs of sub-horizontal tension gash with straight walls. This gash is crosscut by oblique tension gashes with straight walls (sample MAR1_1_676.56). Microphotograph in (**f**) is an inset of (**e**)

(elongate)-blocky microfabrics (red arrow in Fig. 6d) and the rim a fibrous texture. The fibres are perpendicular to the vein wall (blue arrow in Fig. 6d).

Sub-horizontal tension gashes with straight walls are up to 1.5 mm in thickness and also show a typical antitaxial crack-seal microfabric (Fig. 6e,f). These veins are mostly fibrous, with fibres oriented perpendicular to the vein wall as well as bedding plane and occur in relation with calcite slickenfibres. This relationship is further described in Sect. 4.2.2.

4.2.2 Fault planes

4.2.2.1 Normal faults The observed normal faults have dip angles between 15 and 60°. The microstructural investigation reveals three different types of normal faults, with and without macroscopically visible mineralization: (i) Normal faults without mineralization that are characterized by a change in the shape-preferred orientation of the clay minerals within the fault and a reduction in grain size relative to the surrounding matrix (Fig. 7a, b). (ii) Mineralized normal faults that only comprise calcite crack-seal veins parallel to the fault plane (Fig. 7c, d). (iii) Normal faults containing thick (up to 15 mm) secondary precipitates on their fault planes (Fig. 7e–g). These fault planes comprise coarse-grained calcite and quartz-calcite veins, coarse-grained calcite ribbons, and thin celestite ribbons (Fig. 7g). In some cases, these ribbons are deformed (boudinaged). The originally sub-horizontal bedding layers are, in parts, sheared into the fault plane.

4.2.2.2 Strike-slip faults Strike-slip faults with typical dip of about 60° are associated with calcite slickenfibres on their surfaces (Fig. 8a,b). The fault planes typically comprise a 2–3 mm-thick layer of coarse-grained vein calcite, calcite slickenfibres as well as pieces of fibrous calcite veins (Fig. 8c). The slickenfibres with very straight boundaries localize on calcite veins (Fig. 8c). This points towards a multiple deformation/slip-history along these fault planes.

4.2.2.3 Thrust faults Thrust faults commonly overprint pre-existing subhorizontal veins (Fig. 9a–c). In these cases, the thrust-related slickensides with calcite slickenfibres are often observed to localize and thus overprint the former rim of a calcite vein (Figs. 9d–g). However, the slickensides are also observed to overprint the center of the subhorizontal veins (Fig. 9e). The calcite fibres constituting the subhorizontal veins are perpendicular to the slickenfibres and in some cases are bent, indicating a progressive growth in a changing orientation (Ramsay et al., 1983).

4.2.3 Micron-veinlets

Micron-veinlets occur in context with thrust faults and strike-slip faults and have thicknesses between 10 and 100 µm and a wiggly appearance. The micron-veinlets overprint slickenfibres (Fig. 10a) but are also bounded by slickensides and small individual slip planes (Fig. 10b). The micron-veinlets are well visualized by CL microscopy revealing that they overprint slickensides associated with thrust faults and strike-slip faults (Fig. 11). Some micron-veinlets extend outside the slickenfibres into the matrix (Fig. 11d, f). Within the matrix, micron-veinlets can be sheared (Fig. 11f) due to thin slip surfaces. Figure 10e displays microprobe element maps of a micron-veinlet. The region of interest (red box in Fig. 10d) includes a blocky calcite vein and calcite micron-veinlets.

4.3 Vein and slickenfibre geochemistry

EDX point data from the various calcite vein fillings and slickenfibres are shown in Fig. 12. The minor element chemistry (Mg and Fe) reflects two distinct groups of calcite mineralization that also have different structural characteristics: slickenfibres and tension gash fillings. Thereby, slickenfibres in all three samples show by tendency higher Fe and Mg values in calcite compared to tension gash fillings.

The XFM maps provide information about the distribution of Sr and Fe in slickenfibres or veins (Fig. 13). For sample BOZ2_1_531.77, which contains both slickenfibres and fibrous veins, the XFM maps show that calcite slickenfibres yield higher values for both Sr and Fe compared to the fibrous calcite vein directly adjacent (Fig. 13a, b). The distribution of Sr and Fe is homogeneous within the slickenfibres. Within the fibrous parts of the vein, the individual fibres display differences in concentration values as evidenced in the Fe map with different purple values between the fibres. However, the antitaxial fibrous calcite veins show homogeneous concentrations in their 'growth direction'. The micron-veinlets are also well displayed within the synchrotron maps and appear as wiggly stripes with similar concentration values for Sr and Fe as the slickenfibres.

4.4 U–Pb calcite dating

To obtain U–Pb ages of faulting and secondary calcite precipitation, a total of 39 calcites from normal faults, thrust faults, strike-slip faults, and dilative tension gashes were analyzed by LA-ICP-MS. The data are presented in Additional file 1: Table S2 and Additional file 1: Figs. S3-S8.

Unfortunately, all dating attempts were unsuccessful for the following reasons: (a) the isochron did not provide a lower intercept age, (b) large absolute uncertainty, (c) the

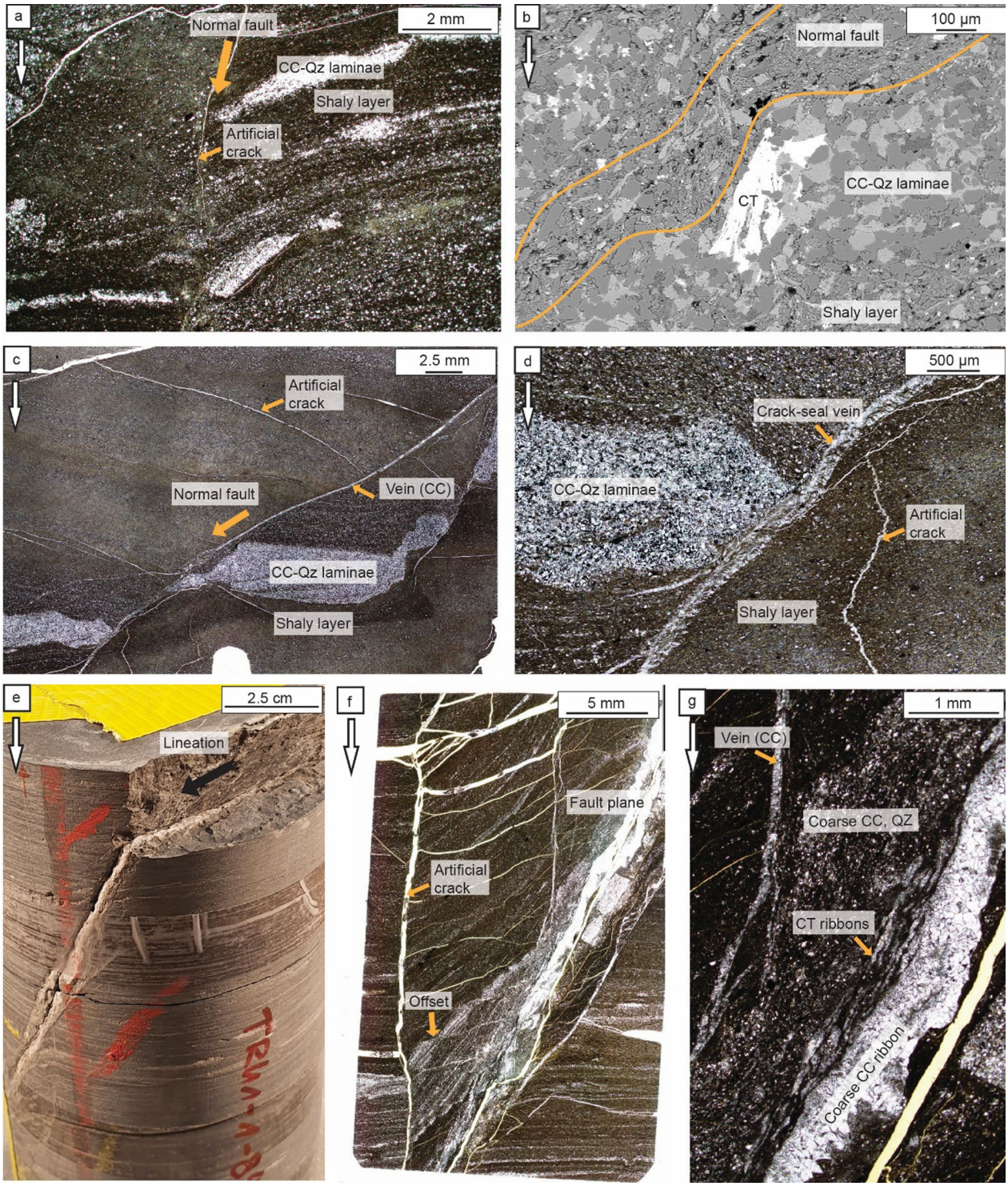

Fig. 7 Overview of macro- and microphotographs from normal faults. **a** Microphotograph of normal fault without mineralization. **b** BSE SEM image of (**a**) shows grain size reduction within the normal fault as well as a change in the shape preferred orientation of the clay minerals, relative to the surrounding Opalinus Clay matrix. **c**, **d** Microphotograph of normal fault with parallel calcite vein cutting the matrix at high angle. **e** Macroscopic image of fault plane with calcite precipitates. **f** Microphotograph of thin section of (**e**) showing the normal fault. Horizontal bedding layers are dragged into the fault plane. **g** Microphotograph of fault plane shows: calcite veins, coarse-grained calcite (CC) and quartz (QZ), celestite (CT) ribbons and coarse-grained CC ribbon. Samples (**a**, **b**) TRU1_1_849.70B, (**c**, **d**) MAR1_1_668.85, (**e**, **f**, **g**) TRU1_1_846.70

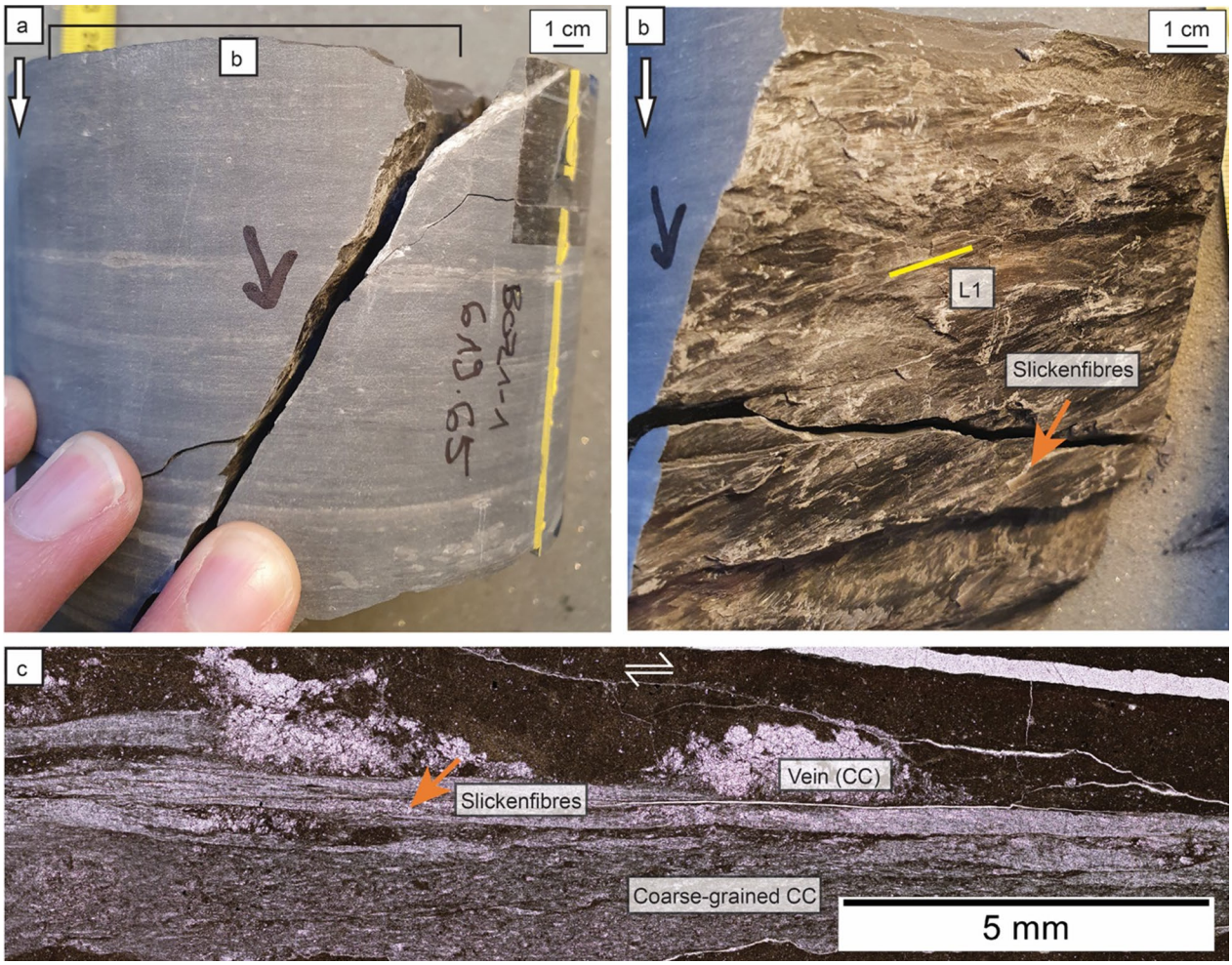

Fig. 8 Macrophotographs and microphotographs of strike-slip fault. **a** Macrophotograph of sample BOZ1_1_619.65 with steep strike-slip fault (dextral). **b** Macrophotograph of strike-slip fault plane with slickenfibres (CC) and lineation (L1). **c** Microphotograph of sample BOZ1_1_619.65 shows that the strike-slip fault plane consists of a layer of coarse-grained calcite and slickenfibres (CC) that localise on calcite veins

lower intercept age was older than the depositional age of the host rock, (d) insufficient robustness of the age trend.

The analysed samples are unsuitable for calcite U–Pb dating because of their consistently low U concentrations and high Pb contents dominated by common (initial) Pb. In these cases, high concentrations of Pb incorporated during calcite precipitation obscure the small amounts of radiogenic Pb produced from decay of U in the time elapsed since the dated event. This effect is evident as the samples in most cases yield $^{238}U/^{206}Pb$ ratios between 0 and 2 and $^{207}Pb/^{206}Pb$ ratios above 0.8 (Additional file 1: Figs. S1–S5). For comparison, the analysed reference materials yield higher $^{238}U/^{206}Pb$ and lower $^{207}Pb/^{206}Pb$ ratios (Additional file 1: Fig. S6) allowing to define precise lower intercept ages. In our experience, secondary carbonates from clay-rich host rocks in most cases yield low U and high common Pb contents and thus, are difficult to date by U–Pb and U-Th geochronology.

4.5 Carbonate clumped isotope thermometry

The stable and clumped isotope data of a representative subset of 18 calcite mineralisations from different structure types and deformation phases across all boreholes are shown in Fig. 14 and Additional file 1: Table S3 in the appendix. Because of their small sizes, no micron-veinlets could be sampled. Reconstructed Δ_{47} temperatures range between 46 ± 8 and 104 ± 9 °C and calculated $\delta^{18}O_{fluid}$ values between -4.7 ± 0.6 and $+3.6 \pm 0.9$ ‰. The Δ_{47} temperatures and $\delta^{18}O_{fluid}$ compositions show substantial variability within individual structure types while across different structure types, the two parameters show largely overlapping ranges with no conclusive pattern (Additional file 1: Table S3). Also, when grouping the samples by compatible deformation phases, Δ_{47} temperatures and $\delta^{18}O_{fluid}$ compositions show more variation within the same deformation phase than between

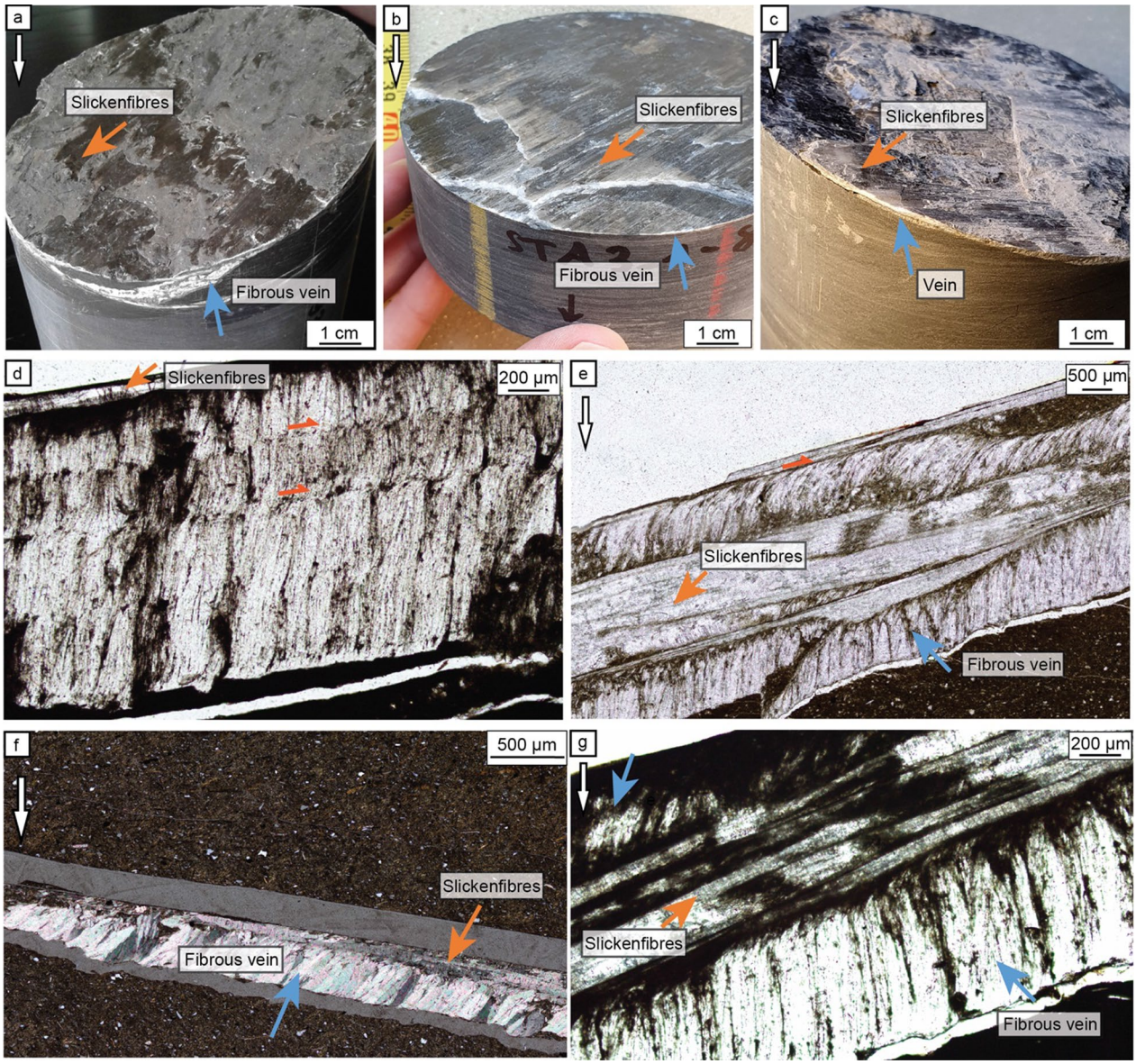

Fig. 9 Three examples of thrust faults associated with subhorizontal and fibrous veins. White arrows indicate downhole arrows. **a**–**c** Macroscopic photographs of thrust faults (with slickenfibres) parallel to fibrous calcite veins (**a**: sample STA2_1_793.15, **b**: sample STA3_1_851.27, **c**: sample BOZ2_1_531.77). **d** Optical light micrograph showing fibrous crack-seal vein, with calcite fibres perpendicular to the slickensides on the upper slip surface (sample BOZ2_1_527.87). **e**–**f** Optical light micrographs showing fibrous veins disrupted by slickensides (in (**e**) sample BOZ2_1_531.77, in (**f**) sample STA2_1_793.15). **g** Optical light micrograph shows multiple slickensides localised on the dip slip surface of a fibrous calcite vein (sample BOZ2_1_531.77)

different deformation phases (Fig. 14). Nevertheless, Δ_{47} temperatures of structures associated with local NE-SW extension are tendentially lower than those of the other deformation phases. However, as the dataset is very limited with only two samples covering NE-SW extension at two drill sites, this observation is not well constrained.

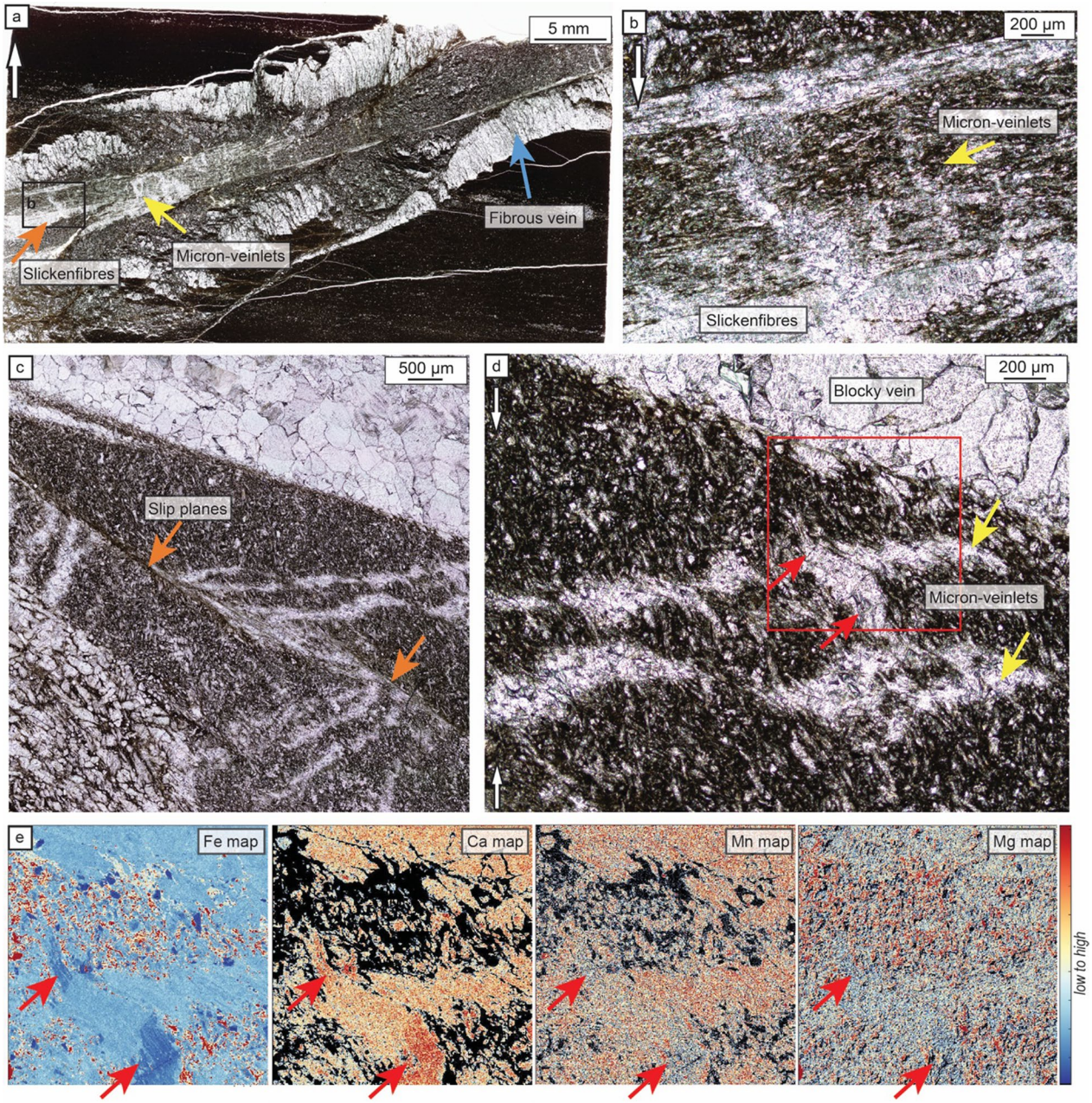

Fig. 10 Overview of optical light micrographs of cm-thick thrust faults showing multiple deformation by formation of veins, slickensides and micron-veinlets. **a** Thin section view of thrust fault constituted by fibrous veins, slickensides as well as micron-veinlets. **b** Zoom in on (**a**) shows slickensides and wiggly micron-veinlets that are bounded by the slickensides. **a**, **b** Includes sample BOZ2_1_482.70A. **c** Thin section view of thrust fault with blocky calcite vein and micron-veinlets bound by small slip planes. **d** Zoom in on (**c**) shows how the micron-veinlets, are sheared by thin slip planes. **c**, **d** includes sample BOZ2_1_507.70. **e** Results of WDS microprobe mapping of red area in (**d**) showing the different element distributions

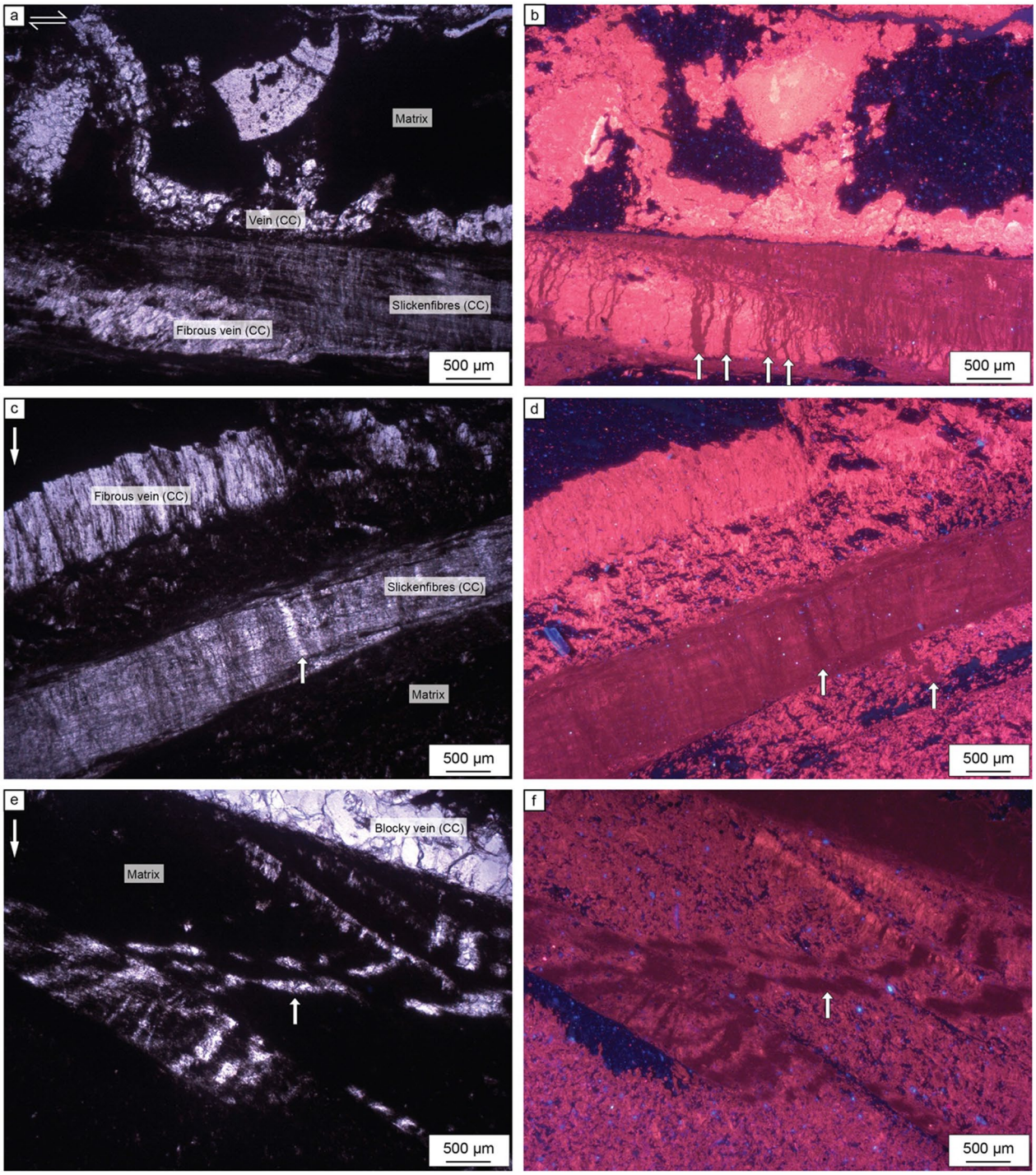

Fig. 11 Micron-veinlets (small white arrow) imaged with optical light microscopy (**a**, **c**, **e**) and identical positions imaged by CL microscopy (**b**, **d**, **f**). **a**, **b** Strike-slip fault, with dextral sense of shear. The calcite slickenfibres are overprinted by many wiggly micron-veinlets (sample BOZ1_1_619.65). **c**, **d** Thrust fault associated with a fibrous calcite vein. The slickensides on the fault plane are overprinted by wiggly calcite micron-veinlets (sample BOZ2_1_507.70). **e**, **f** Thrust fault with micron-veinlets sheared by slip planes in the matrix (sample BOZ2_1_482.70A)

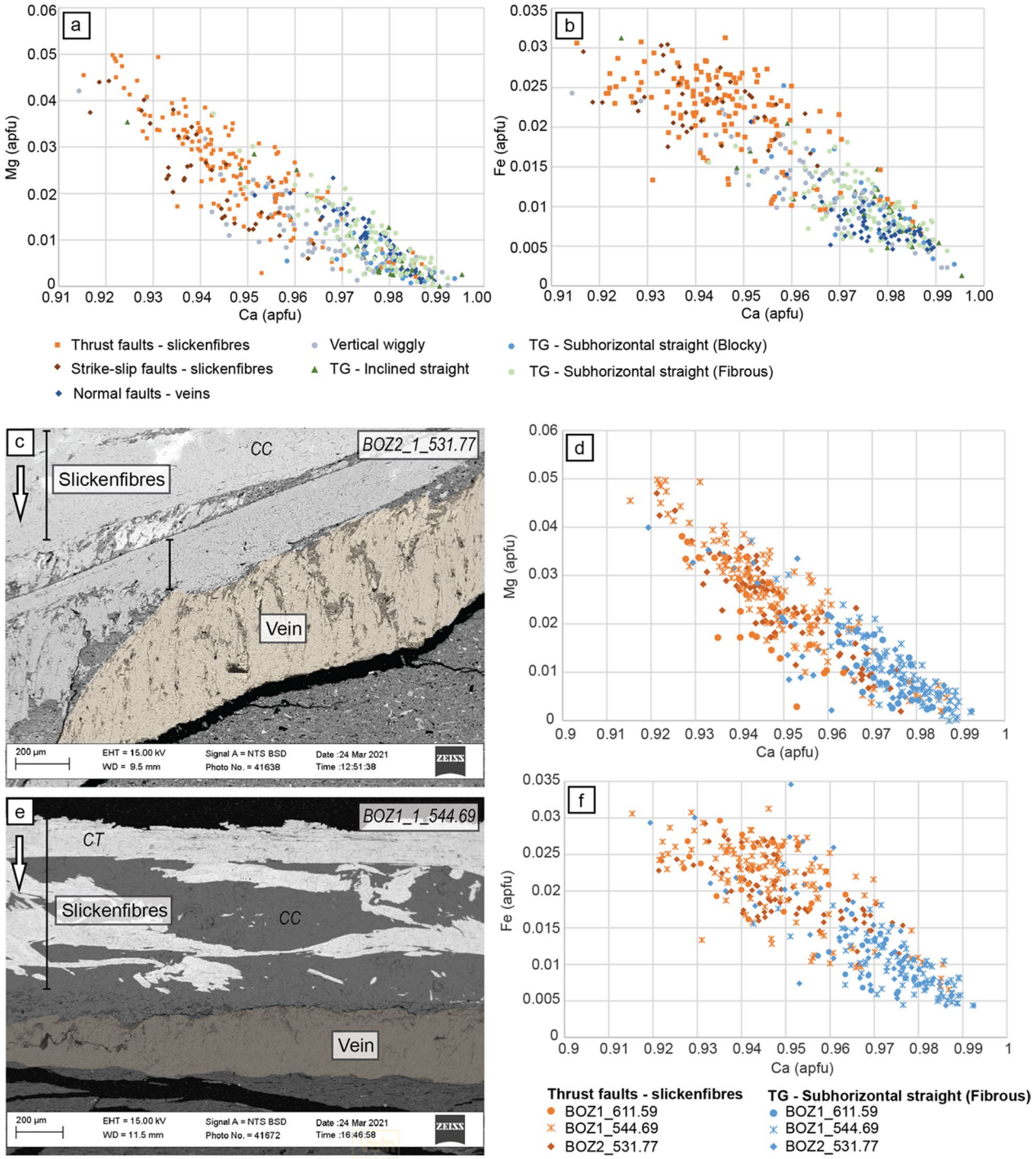

Fig. 12 EDX point data of microstructures including calcite mineralization. **a**, **b** Calcite slickensides show distinct group of compositions with higher Fe and Mg values than calcite in other tension gash fillings. TG: tension gash. Data included from the following samples: BOZ2_1_527.87, BOZ2_1_530.16, BOZ2_1_548.59, BOZ2_1_541.82, STA3_1_830.87, BOZ1_1_544.69, BOZ2_1_531.77, BOZ1_1_613.58. **c**–**f** Local microstructural analyses of sample BOZ2_1_531.77 and sample BOZ1_1_544.69 show similar groups of: calcite slickensides on thrust faults with higher Mg and Fe values compared to fibrous calcite veins directly adjacent to the slickensides

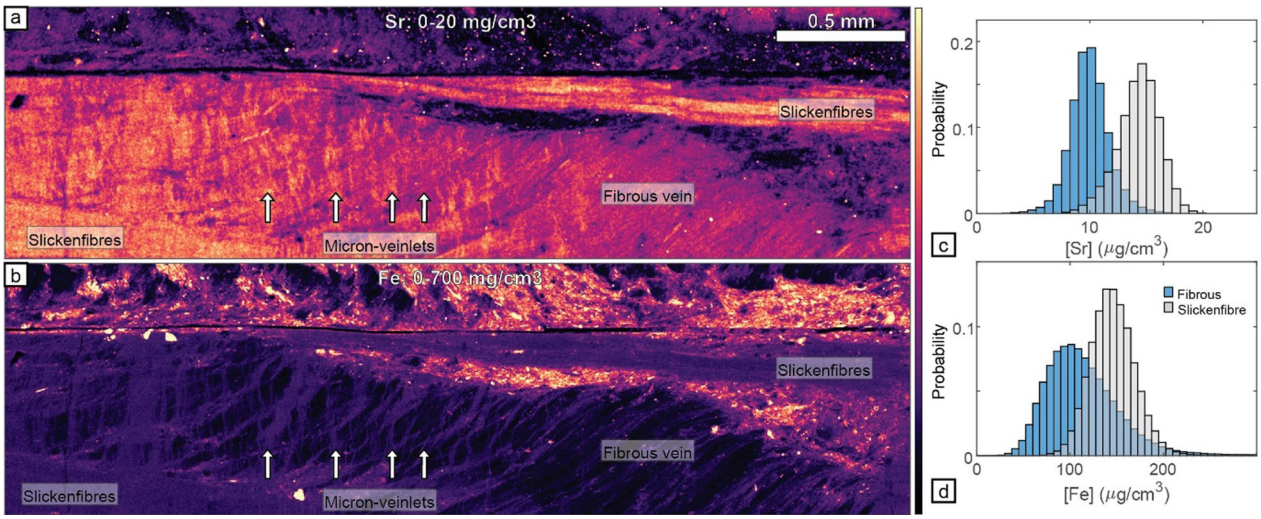

Fig. 13 XFM trace element maps. **a-b** Sr and Fe map of sample BOZ2_1_531.77. Concentration values according colour bar: dark colours for low concentration values, bright colours for high concentration values. The image displays calcite slickensides with relative high Sr and Fe values compared to the fibrous calcite veins (see confirmation by histograms in **c**–**d**). The calcite fibres do show homogeneous trace element concentrations (both Sr and Fe) along their growth direction. The micron-veinlets are displays as wiggly stripes cross cutting both slickensides and veins and appear in similar trace element concentrations compared to the slickensides

5 Discussion

5.1 Formation of structure types in the Opalinus Clay

In this section, we discuss the formation mechanisms and timing as well as mineralization temperatures for the different structure types. Regarding deformation timing, U–Pb dating did not provide meaningful absolute deformation ages. However, microstructural imaging revealed evidence for the cyclicity of fracturing processes and subsequent mineralization, thus providing relative age constraints.

5.1.1 Early extensional fractures

Micro-scale tension gashes were identified in all analyzed Opalinus Clay drill core sections. These are dilative brittle structures indicative for the presence of fluids and mineralization after fracturing that led to their complete

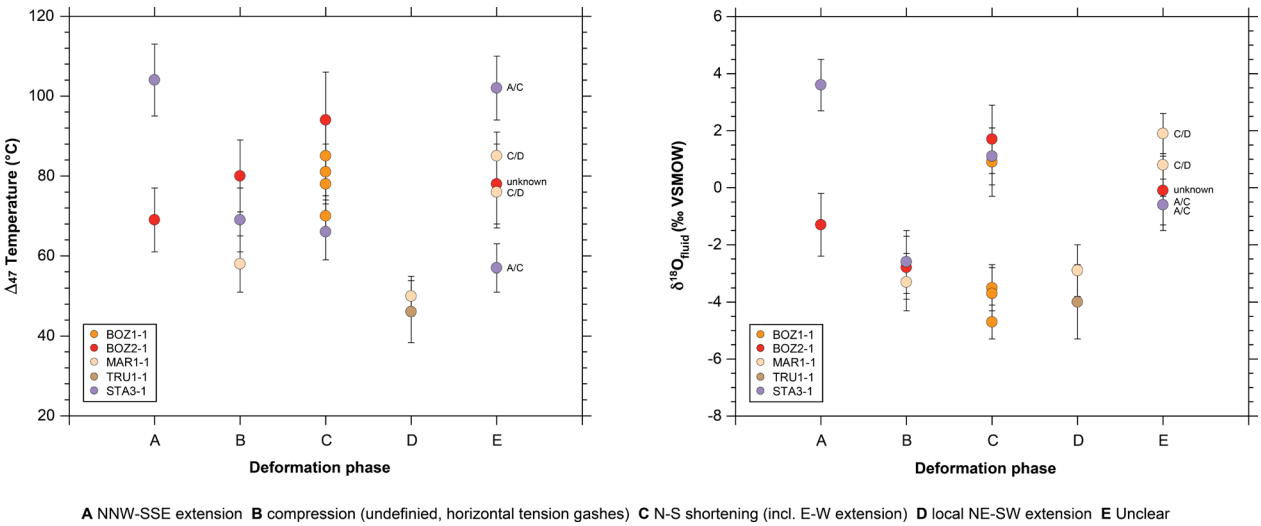

Fig. 14 Δ_{47} temperatures and $\delta^{18}O_{fluid}$ compositions of analysed secondary calcites arranged by corresponding deformation phases. The colour coding indicates different drill sites (cf. Fig. 1 for location)

closure. Three types of tension gashes were observed: (i) vertical wiggly, (ii) bedding-parallel sub-horizontal straight and (iii) inclined straight types.

(i) The first type includes vertical fibrous veins with a wiggly appearance that do occur in all studied drill cores. These vein types are antitaxial and the repeated crack-seal fracturing occurred at the interface between calcite and Opalinus Clay. Although this wiggly appearance at first glance yields the impression of ptygmatic folding (Fig. 6a,b), deformation by folding can be discarded. In case of folding, one would expect the calcite fibres to be deformed around the apparent 'fold hinges'. Instead, the fibres are consistently horizontal, oriented bedding-parallel and parallel to each other. This observation together with the vertical tension gash orientation implies a constant kinematic framework with vertical sigma 1 and horizontal sigma 3 allowing for horizontal tension gash opening during their formation. It is therefore proposed that the wiggly shape of these mineralized tension gashes derives from the initial fracture and crack propagation process in a sediment compaction framework. At this stage, obstacles such as quartz and feldspar grains in the Opalinus Clay matrix served as mechanical stiff inclusions with compaction-induced stress concentrations in their vicinity. Crack propagation occurred therefore in the mechanically weak clay matrix by deflecting around the rigid obstacles. Clumped isotopes show that these fractures must have formed at temperatures around 70 °C (Additional file 1: Table S3) sometime between early soft sediment compaction and the second type of veins (see below). Low temperature fracturing and associated calcite precipitation (< 80 °C) in clay units is known from paleo-accretionary wedges (Dielforder et al., 2015, 2016, 2022). However, under the fluid saturated, highly

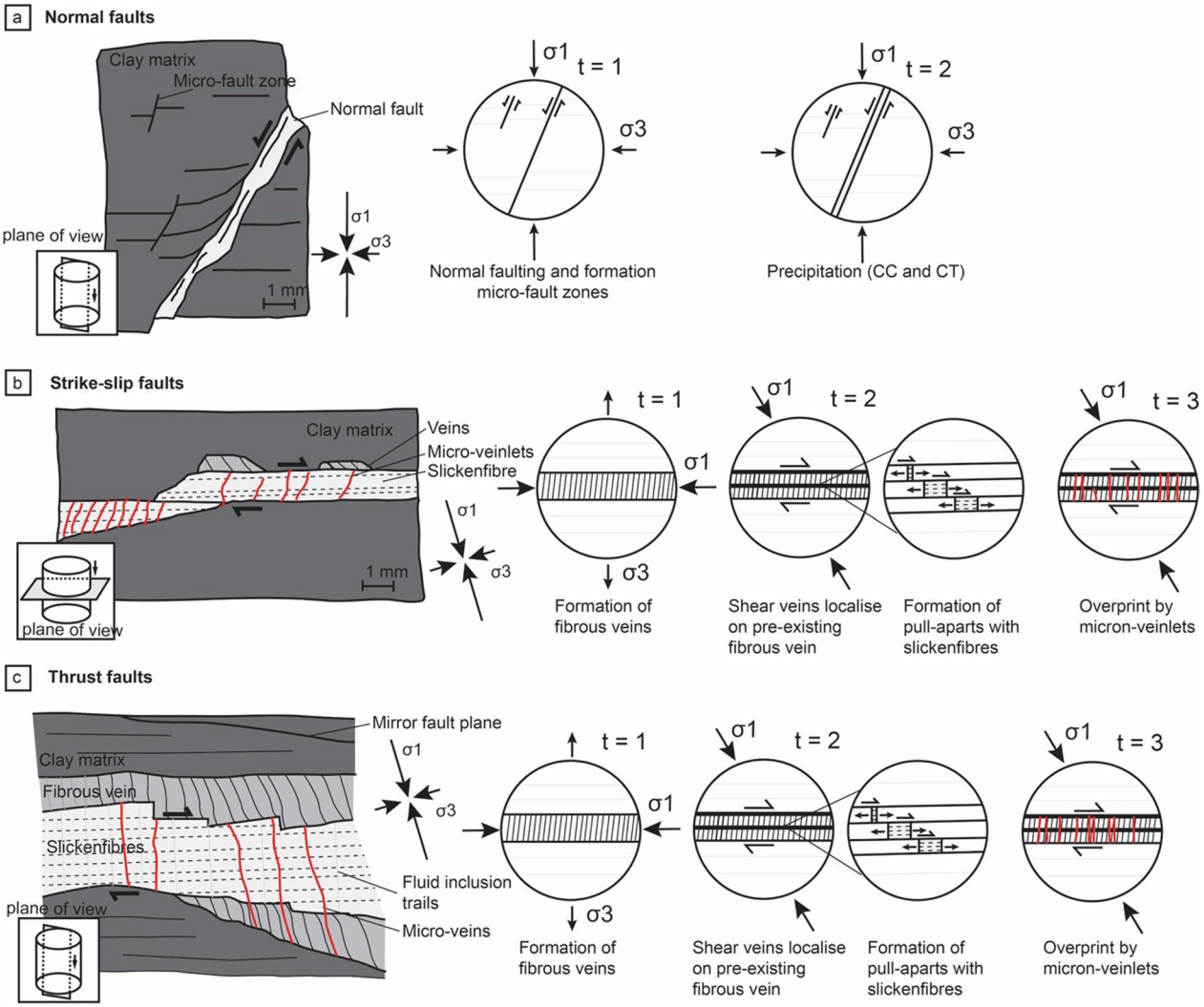

Fig. 15 Sketch of main fault pane types related to the different tectonic regimes and interpretive relative timing of deformation phases

dynamic and critically stressed conditions in accretionary wedges, commonly straight and planar vein rims occur, pointing to fast fracture processes. This contrasts to the wiggly veins observed in the Opalinus Clay. It is therefore assumed that slow crack propagation and fracture opening allow cracks to migrate around obstacles instead of dissecting them.

The second group of tension gashes are the (ii) sub-horizontal types, which show microstructural/geochemical similarities with the third group (iii) that include inclined tension gashes showing angles < 50°to the bedding. The mineralization of tension gashes from group (ii) and (iii) both consists either of elongate-blocky shaped calcite or fibrous calcite and are interpreted as antitaxial crack-seal calcite veins (Fig. 6c–f). The geochemical composition measured of both groups of tension gashes is very similar as evidenced by their narrow grouping in the EDS data plots (Fig. 12).

The sub-horizontal veins point to a vertical extension and a horizontal shortening direction, which requires a change in stress field with respect to the formation kinematics of the vertical wiggly tension gashes (i). The Opalinus Clay's internal weak compositional anisotropies affected the formation of these tension gashes as inferred from their bedding (sub)parallel nature. Opalinus Clay with pore fluid pressures being close to lithostatic loading conditions could have favoured bedding (sub)parallel initial fracturing and subsequent tension gash opening (e.g., Sibson, 1981). The crack-seal texture of the sub-horizontal tension gashes indicates a repeated and cyclic fracturing and healing by precipitation of fibrous calcite (e.g., Bons et al., 2012; Ramsay, 1980). In general, aperture opening during individual fracturing events are small, followed by precipitation of calcite. Hence, it is probable that for all observed crack-seal veins, the crack-sealing mechanisms occur rather slow (e.g., Muller et al., 2000). The inclined tension gashes often form as dilative structure on normal fault planes and therefore their kinematic framework is related to the formation of faults (Fig. 15).

5.1.2 Small-scale faults

The observed faults share the common characteristic of non-coaxial but highly localized deformation. Under such conditions, claystones, such as the Opalinus Clay, represent preferential sites for detachment horizons owing to their low mechanical strengths. These faults are also called 'décollement zones' and are found in clay-rich sediments of accretionary prisms such as Barbados (Housen et al., 1996; Labaume et al., 1997), the Tohoku subduction zone (Chester et al., 2013) and in the European Alps (Dielforder et al., 2015, 2016). A prominent and intensely studied example is the Opalinus Clay hosted 'Main Fault' in the Mont Terri rock laboratory (Jaeggi et al., 2018; Laurich et al., 2014, 2017, 2018; Orellana et al., 2022; Wenning et al., 2021). There, diagnostic deformations structures such as clay gouge, scaly clay, mirror-like fault planes, slickenfibres and veins have been described (Laurich et al., 2014, 2017, 2018). In our study, however, we did not observe fault gouges in the studied Opalinus Clay drill cores and also scaly clay was macroscopically not detectable. Hence, deformation structures indicative of non-coaxial deformation exclusively consist of fault planes with slickenfibres (Figs. 8, 9, 10, 11, 12, 13, 14). They appear as cm-sized discrete fault planes, either without (mirror-like fault planes) or with mineral precipitates (slickenfibres: calcite and minor celestite). In the case of mirror-like fault planes, the clay mineral enriched thin (< 100-10 µm) seams represent the principal slip planes as indicated by the striae on their slip surfaces. In addition, the grain sizes must be reduced, and the clay content increased in the mirror-like fault planes compared to the Opalinus Clay matrix. For these reasons, a combination of re-orientation of clay minerals, pressure solution, shearing and grain size reduction is inferred to be occurring during formation of the mirror-like fault planes (Laurich et al., 2014). Hence, mirror-like fault planes can be considered to represent compactional domains which formed under the presence of fluids and shearing but without or with only limited dilatational deformation. This contrasts calcite and celestine slickenfibres clearly indicating dilatational deformation combined with mineral precipitation during shearing. Being dilative they are certainly underpressured relative to the adjacent matrix, which both promotes supersaturation and calcite precipitation but also fluid movement into the dilatant fault zone. Slickenfibres always occur together with the clay-rich seams already described in the case of mirror-like fault planes but also with bedding parallel and inclined tension gashes. This fits with observations of Guglielmi et al., (2015, 2017) that show that shear failure only occurs once the injection pressure reached levels that would be conducive to local dilatant opening. We assume a strong mechanical control on the nucleation of slickenfibres in the case of Opalinus Clay as observed by Leflèvre et al. (2016) for a Toarcian shale (Fig. 15b). The strength contrast between the rheologically weak Opalinus Clay and calcite-bearing, and therefore comparatively stiffer veins, obviously controlled nucleation, and strain localization of the slickenfibres. Slickenfibres precipitate in small pull apart structures. Due to progressive shear parallel to the bedding, pore space is provided in which calcite precipitates on pre-existing calcite grains (Fig. 15b, c). In this way, long but thin single crystals evolve in the shear veins (e.g., Passchier & Trouw, 2005; Peacock & Sanderson, 1995). Incipient deformation in claystones is thought to localize in very thin (micro-scale)

zones that form a mechanical weakness (Agar et al., 1989; Dehandschutter et al., 2004; Ishii, 2012; Laurich et al., 2014, 2017; Winhausen et al., 2021, 2022).

Closely related to the slickenfibres on fault planes is the appearance of micron-veinlets reflecting late-stage tension gashes (Fig. 15c). the micro-veinlets are only developed within the calcite (slickenfibre) veins, ca. perpendicular to the vein wall, and do not extend into the Opalinus Clay matrix. This would be explained by the expected refraction of the principal stress axes into orientations nearly perpendicular and parallel to the interface between a strong layer and a weak matrix that is being stretched, as well as the dynamic or tectonic "underpressure" in the stretched stronger layer, promoting mode I extensional brittle failure (Mancktelow, 1993, 2008). The fact that they perpendicularly dissect (sub)horizontal bedding parallel veins (Fig. 11) implies horizontal stretching of the latter most likely simultaneous to shearing along slickensides/mirror-like fault planes. In some cases, even slickensides themselves become dissected by micron-veinlets (Fig. 11). This is interpreted as earlier slickenfibre generations, the shear deformation of which was deactivated and exposing the slickenfibres to horizontal stretching, while shear deformation occurred on a different slip level above or below (Fig. 11). This inference is corroborated by the observation that micron-veinlets are occasionally being found to be sheared themselves along an even younger generation of slickensides.

Hence, although micron-veinlets always represent the youngest dilative veining event within an individual subhorizontal vein structure, their orientation being perpendicular to the slickenfibre (veins) does suggest that there needs to be a switch in the principal stress axes indicating two kinematically separated events for these two orthogonally oriented vein types.

The pronounced differences in element distributions between fibrous veins and slickensides, with the increased Mg, Fe, and Sr concentrations in the latter (Figs. 12 and 13), can have two potential causes: (1) Different fluid sources with a different original geochemical signal or (2) differences in the precipitation kinetics of calcite. Fluids can be intraformational or externally derived and it is known that the degree of oversaturation of fluids depends on the opening rate and associated drop in pore fluid pressure as well as on the growth kinetics of calcite (Berger & Herwegh, 2019; Pacquette & Reeder, 1995; Teng et al., 2000; Vernon, 2004). At the current stage, however, we do not have enough data to promote or exclude one of the two scenarios and this will be discussed in detail elsewhere. While fibrous veins document small incremental openings (Bons et al., 2012; Ramsay, 1980), slickenfibres might relate to stages of instantaneous slip with associated fast drops in pore fluid pressures, potentially yielding in enhanced incorporation of Fe, Mg, and Sr. Independently of which of the two scenarios holds, the fact that these elemental differences are consistent over all three sitings would either indicate a regional behavior in the case of (1) or a consistent phenomenological precipitation behavior in the case of (2).

5.2 Calcite trace element geochemistry, burial temperatures, and δ18O compositions of precipitating fluids

The wide range of fluid temperatures and oxygen isotopic compositions ($\delta^{18}O_{fluid}$) calculated from vein calcites in the Opalinus Clay results from the complex burial history of central northern Switzerland including two cycles of burial and exhumation since deposition of the Opalinus Clay.

Previous estimates for maximum temperatures during the first interval of deep-burial during the Late Jurassic and Cretaceous range between 85 °C for the top of the Opalinus Clay (Mazurek et al., 2006) and around 115 °C for the lower part of the Staffelegg Formation, few tens of metres below the Opalinus Clay (Looser, 2022). The differing maximum burial temperature estimates mainly reflect the different proxies used in the two studies. Temperature estimates of Mazurek et al. (2006) are based on combined apatite fission tracks, vitrinite reflectance, and maturation-dependent biomarkers, all of which yielding integrated temperature signals recorded over longer time periods of the burial history. Accordingly, temperature signals recorded by these proxies may be influenced by later burial, which makes temperature estimates in early stages of the burial history challenging and short-lived thermal events are not always detectable. In contrast, clumped isotope thermometry provides burial temperatures at specific points in time and thus allows to record short-lived temperature anomalies not recorded by other geochronometers, provided that secondary carbonates formed during such events (e.g., Brigaud et al., 2020). Temperatures ranging between 69 ± 8 and 104 ± 9 °C obtained from structures compatible with regional NNW-SSE extension (Fig. 13), which coincides with the first burial interval during Late Jurassic to Cretaceous times, are thus in agreement with the previous burial temperature estimates of Mazurek et al. (2006) and Looser (2022). Estimates for maximum burial temperatures of the Opalinus Clay during the second interval of deep-burial during Late Miocene are approximately 65 °C (Mazurek et al., 2006). This was confirmed by Looser et al. (2021) who reconstructed formation temperatures between 50 and 80 °C of calcite mineralisations on thrusts and strike-slip faults hosted by Middle Jurassic and Middle Triassic rocks in the eastern Jura Mountains. Temperatures from structures in the Opalinus

Clay compatible with N-S shortening and E-W extension coinciding with the second interval of deep burial, yield temperatures between 70 ± 5 and 94 ± 12 °C. This temperature range is higher than previous temperature estimates for this time interval. The formation timing of horizontal tension gashes remains unconstrained and a sound interpretation of Δ_{47} temperatures is thus impossible. Similarly, grouping into deformation phases for structures compatible with local NE-SW extension is not unequivocally clear and interpretations of Δ_{47} temperatures remain speculative.

Regarding $\delta^{18}O_{fluid}$, the obtained values between − 4.7 ± 0.6 and + 3.6 ± 0.9 ‰ across all deformation phases reflect a wide range of different fluid compositions. In some cases, negative $\delta^{18}O$ signatures of meteoric waters are at least partly preserved whereas in other cases, positive values reflect extensive fluid-rock interaction at elevated temperatures. As there are no systematic differences in $\delta^{18}O_{fluid}$ between deformation phases, and the timing of vein formation can only be qualitatively estimated, no conclusions regarding the source of fluid (internally vs. externally derived) can be drawn at this point. A fluid interacting with the same host rock at different temperatures will show different $\delta^{18}O_{fluid}$ compositions (i.e., more heavy values at higher temperatures). Accordingly, a local fluid that evolves within the Opalinus Clay, will show different $\delta^{18}O_{fluid}$ values during different stages of the thermal history and variations in $\delta^{18}O_{fluid}$ do not necessarily reflect different fluid sources. Therefore, for the Opalinus Clay in central northern Switzerland, $\delta^{18}O_{fluid}$ alone is not an unambiguous proxy for the fluid source. It should be combined with other geochemical tracers such as C and Sr isotopes as well as coupled U–Pb-$\delta^{18}O_{fluid}$ datasets from the confining units and interpreted within the context of the local and regional paleo-hydrogeological evolution.

5.3 Structural geological interpretation

The investigated boreholes provide a unique opportunity to investigate the spatial distribution of natural fractures within Opalinus Clay. It should be noted that all boreholes were drilled more than 100 m away from known regional fault zones (Fig. 1) Nevertheless, it is valuable to mention that hardly any discrete larger-scale faults that transect the bedding with displacements exceeding the dm scale were encountered in the drill cores. Reported offsets are consistently below 30 mm with an average of about 10 mm (58 offset measurements). This is in stark contrast to other more brittle units that comprise rocks with higher cohesion compared to the Opalinus Clay (Nagra, 2021a, 2021b, 2021c, 2022a, 2022b, 2022c, 2022d, 2022e, 2022f). The units at least sporadically show deformation structurs with larger displacemnets. These observations hint towards a specific deformation behaviour

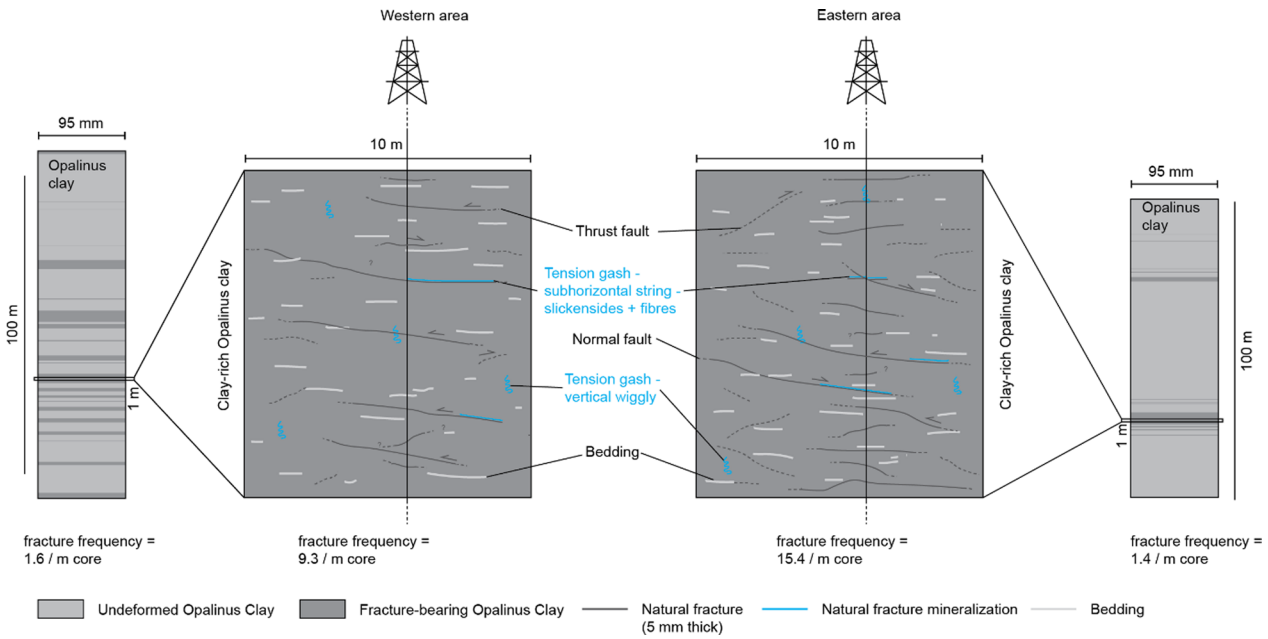

Fig. 16 Conceptual structural geological sketches for the deformation style of Opalinus Clay for the far eastern and western parts of the study area. Note that these sketches focus on m-scale zones within the over 100 m thick formation that is elsewhere often free of natural fractures over several tens of m

of Opalinus Clay also observed at larger scale (e.g., in seismic data; Roche et al., 2020). It is inferred that this is due to this rock's rheological/geomechanical properties and possibly the local stress conditions in northern Switzerland. According to numerical stress models (Hergert et al., 2015), the pronounced mechanical stratigraphy in this region of the external Alpine foreland leads to stress concentrations in the rheologically more competent units above and below the Opalinus Clay rather than within the Opalinus Clay itself. Despite this setting a wide variety of small-scale natural fractures were recognized in the drill cores investigated here, whose structural geological significance requires further discussion.

The only occasionally observed vertical wiggly veins were most often found to be of short extent. Tectonically, these fractures are therefore considered to be of minor significance. The other mineralized tension gashes and small-scale fault types exceed the core diameter (95 mm) so their lateral extent (e.g., length) remains unknown. With the exception of the two boreholes in the very west of the study area (BOZ-1 and BOZ-2; cf. Figs. 1 and 5) they occur clustered within diffuse deformation zones whose apparent width is in the range of several m (BAC1-1, STA3-1, STA2-1, BUL1-1, MAR1-1 and TRU1-1; Fig. 5). In this regard, there are no indications that this deformation is bound to certain lithostratigraphic units within the Opalinus Clay. Beside the above-mentioned "veins", another frequent natural fracture type within the Opalinus Clay that does not feature secondary mineralization and was not investigated microstructurally in the context of this study are mirror-like fault planes typically developed parallel to the sedimentary bedding. These structure types were recognized over the entire cores and appear slightly less strongly clustered than the aforementioned veins. Because of their bedding parallel orientation, the lack of markers and the limitation of the diameter of the drill core, no indications on the lateral extent of these structures can be drawn from the drillcores.

The integrative interpretation of these individual observations at drillcore-scale lead us to suggest a larger scale structural geological model for the Opalinus Clay of central northern Switzerland illustrated in Fig. 16. It is suggested that strain is expressed by occasional occurrence of deformation zones within the formation that are characterized by the clustered occurrence of small-scale fractures with secondary calcite mineralization. It is presumed that this clustering of "veins" is due to the repeated reactivation of these rheological discontinuities within the Opalinus Clay during the polyphase tectonic evolution of the region as also suggested by the geochemical differences observed when comparing veins and slickenfibres in direct vicinity. Evidence for the importance of brittle strain relocation along pre-exiting discontinuities in the otherwise rheologically weak Opalinus Clay is given by observations at the microscopic scale (Fig. 6e, f in MAR1-1) and on the macroscopic scale (for example within the occasionally encountered more complex fault zones featuring multiple slip increments cf. Sect. 4.1; zones at around 911 m MD in BAC1-1, around 850 m MD in STA 2–1; Decker et al., 2022; Nagra, 2022d, 2022e) and very frequently at the microscopic scale (Fig. 6e, f in MAR1-1).

On the regional scale, some differences in deformation style can be observed. Towards the eastern boundary of the study area, extensional deformation zones appear to be more common, likely due to the increasing proximity to the transtensional Hegau-Lake Constance Graben (Egli et al., 2017). In contrast, the western part of the study area is dominated by horizontal shortening (compressional) structures with subhorizontal principal stress direction that is largely related to the formation of the Jura fold-and-thrust belt further to the south (Madritsch, 2015). In the very west (characterized by the boreholes BOZ-1 and BOZ-2), the Opalinus Clay appears to be more pervasively deformed by these structures. This may be an indication that the Opalinus Clay in this area is more strongly tectonically overprinted, which is in line with the independent observation that regional shortening in relation to Alpine foreland convergence gradually increases from east to west (Burkhard, 1990; Malz et al., 2016).

6 Conclusion

An extensive drilling campaign aiming at further characterizing the Mid-Jurassic Opalinus Clay for radioactive waste disposal resulted in a unique drill core data set to study natural deformation structures, both macroscopically and microscopically. Locally, small-scale (cm-sized) fractures occur in the drill cores that are sometimes associated with secondary mineral precipitates. The latter are generally referred to as veins and encompass various types of tension gashes and small-scale mineralized faults.

The microstructures as well as the chemical composition of these veins indicate polyphase deformation. While a direct dating attempt of the secondary calcite by U–Pb dating failed, the detailed structural mapping allows for the discrimination of relative age constraints from the structural orientations and fault slip kinematics. Accordingly, the earliest veins formed already during sediment compaction (Jurassic times), while the relatively youngest ones are likely to relate to Neogene Alpine foreland deformation. It appears that during this late tectonic event, fault slip localised on pre-existing and

rheologically stiff discontinuities in the otherwise comparably weak Opalinus Clay.

The significance of the structural drill core observations for the larger scale is intrinsically limited. A conceptual model is proposed which suggests local and occasional occurrences of deformed intervals within the Opalinus Clay. Such deformation zones are characterized by the clustered occurrence of small-scale fractures partly with secondary calcite mineralization. It is further presumed that this clustering of veins is due to the repeated reactivation of these rheological discontinuities within the Opalinus Clay during the polyphase tectonic evolution of the region.

Differences in deformation style observed across the various boreholes can be related to variations in the regional tectonic setting. While in the east, close to the transtensional Hegau-Lake Constance Graben, extensional deformation zones appear to be more common, the western part of the study area close to the Jura Main Thrust show a more pervasive overprint by compressional structures.

Our study provides sound evidence for cyclic deformation within the Opalinus Clay during past tectonic events. However, the clumped isotope dataset presented here does not allow to reconstruct the origin of the fluids from which the vein-filling mineralizations in the Opalinus Clay precipitated. Further investigations in this regard will require more detailed geochemical analyses of samples not only from the Opalinus Clay but also from its confining units, as well as their interpretation within the context of the local and regional paleo-hydrogeological evolution.

Supplementary Information

The online version contains supplementary material available at https://doi.org/10.1186/s00015-023-00438-z.

Additional file 1. Table S1. Overview of all analyzed samples for this study. **Table S2.** U-Pb lower intercept ages with the uncertainty reported as 2s together with additional 2% relative to account for inter-session variability. **Table S3.** Stable and clumped isotope data of secondary calcites. **Figure S1.** Indication of the sawing plane and selection of thin section. **Figure S2.** Macrophotographs of each individual sample. Each sample is displayed in original position; from bottom to top of the core. **Figure S3.** Tera-Wasserburg concordia diagrams of analysed microstructures from the Bözberg 2 borehole. **Figure S4.** Tera-Wasserburg concordia diagrams of analysed microstructures from the Bözberg 2 borehole. **Figure S5.** Tera-Wasserburg concordia diagrams of analysed microstructures from the Marthalen 1 borehole. **Figure S6.** Tera-Wasserburg concordia diagrams of analysed microstructures from the Stadel 2, Stadel 3, and Trüllikon boreholes. **Figure S7.** Tera-Wasserburg concordia diagrams of analysed microstructures from the Stadel 2, Stadel 3, and Trüllikon boreholes. **Figure S8.** Pooled agesand weighted averagesof the secondary reference materials ASH-15D, JTand PDF-9B.

Acknowledgements
We would like to thank Teo Neuenschwander for his assistance during rock sample preparation and Thin Section Lab in Toul (France) for thin section preparation. Further, we would like to express our gratitude for everyone involved in Nagra's deep drilling campaign who provided exceptional core material and core mapping. In particular Michael Gysi, Mona Stockhecke and Hanspeter Weber for leading the drill site geology and the highly capable team mapping carefully every single fracture in each core. Synchrotron X-ray fluorescence microscopy (XFM) was undertaken on the X-ray Fluorescence Microscopy (XFM) beamline at the Australian Synchrotron, part of ANSTO. Furthermore, we would like to thank Lisa Winhausen and an anonymous reviewer for providing careful and constructive paper revisions.

Author contributions
MH, HM and VA designed the project. HM and MH supervised the project. AE and KD executed the structural analyses on the drillcores. IVA prepared the rocks for thin sectioning, performed the microstructural analyses as well as SEM EDX measurements. U–Pb dating was performed by NL together with MG. Clumped isotope data was acquired by NL and interpreted with the help of MM and LA. MG and SB offered their lab facilities for the stable isotope as well as U–Pb analyses. Synchrotron data were acquired by IVA, MWMJ, CS and AL. IVA, RS and HM integrated all data, prepared figures and wrote the manuscript with contributions from MH and NL.

Funding
Open access funding provided by Swiss Federal Institute of Technology Zurich. This project was funded by the Swiss National Cooperative for the Disposal of Radioactive Waste (Nagra).

Availability of data and materials
The datasets generated and/or analyzed during the current study are available in the supplementary data file.

Declarations

Ethics approval and consent to participate
Not applicable.

Consent for publication
Not applicable.

Competing interests
The authors declare that they have no competing interests.

Author details
[1]Institute of Geological Sciences, University of Bern, Bern, Switzerland. [2]Present Address: Department of Earth Sciences, Geological Institute, ETH Zürich, Zürich, Switzerland. [3]Swiss National Cooperative for the Disposal of Radioactive Waste (Nagra), Wettingen, Switzerland. [4]Present Address: Swisstopo, Wabern, Switzerland. [5]Department of Earth Sciences, ETH Zürich, Zurich, Switzerland. [6]Department of Geology, Universität Wien, Vienna, Austria. [7]Geo Explorers AG, Wasserturmplatz 1, 4410 Liestal, Switzerland. [8]School of Earth and Atmospheric Sciences, Centre for Data Science, Planetary Surface Exploration, QUT, Brisbane, QLD 4000, Australia. [9]Australian Nuclear Science and Technology Organisation, Australian Synchrotron, Victoria 3168, Australia.

Received: 20 November 2022 Accepted: 4 June 2023
Published online: 29 June 2023

References

Agar, S. M., Prior, D. J., & Behrmann, J. H. (1989). Back-scattered electron imagery of the tectonic fabrics of some fine-grained sediments: Implications for fabric nomenclature and deformation processes. *Geology, 17*(10), 901–904.

Anderson, N., Kelson, J. R., Kele, S., Daëron, M., Bonifacie, M., Horita, J., Mackey, T. J., John, C. M., Kluge, T., & Petschnig, P. (2021). A unified clumped isotope thermometer calibration (0.5–1,100 C) using carbonate-based standardization. *Geophysical Research Letters, 48*(7), e2020GL092069.

Berger, A., & Herwegh, M. (2019). Cockade structures as a paleo-earthquake proxy in upper crustal hydrothermal systems. *Scientific Reports, 9*(1), 9209.

Bernasconi, S. M., Daëron, M., Bergmann, K. D., Bonifacie, M., Meckler, A. N., Affek, H. P., Anderson, N., Bajnai, D., Barkan, E., & Beverly, E. (2021). InterCarb: A community effort to improve interlaboratory standardization of the carbonate clumped isotope thermometer using carbonate standards. *Geochemistry, Geophysics, Geosystems, 22*(5), e2020GC009588.

Bernasconi, S. M., Hu, B., Wacker, U., Fiebig, J., Breitenbach, S. F., & Rutz, T. (2013). Background effects on Faraday collectors in gas-source mass spectrometry and implications for clumped isotope measurements. *Rapid Communications in Mass Spectrometry, 27*(5), 603–612.

Birkhäuser, P., Roth, P., Meier, B., & Naef, H. (2001). 3D Seismik: Räumliche Erkundung der mesozoischen Sedimentschichten im Züricher Weinland: Nagra Technical Report. NTB 00-03, Wettingen, Switzerland.

Bock, H., Dehandschutter, B., Martin, C. D., Mazurek, M., Haller, A. D., Skoczylas, F., & Davy, C. (2010). Self-sealing of fractures in argillaceous formations—Evidence, mechanisms and implications for performance assesment (an NEA Clay Club project).

Bons, P. D., Elburg, M. A., & Gomez-Rivas, E. (2012). A review of the formation of tectonic veins and their microstructures. *Journal of Structural Geology, 43*, 33–62.

Bossart, P., Bernier, F., Birkholzer, J., Bruggeman, C., Connolly, P., Dewonck, S., Fukaya, M., Herfort, M., Jensen, M., & Matray, J.-M. (2017). Mont Terri rock laboratory, 20 years of research: Introduction, site characteristics and overview of experiments. *Swiss Journal of Geosciences, 110*(1), 3–22.

Brigaud, B., Bonifacie, M., Pagel, M., Blaise, T., Calmels, D., Haurine, F., Landrein, P., Geops, S., & Paris-saclay, U. (2020). Past hot fluid flows in limestones detected by Δ 47 –(U-Pb) and not recordedby other geothermometers. *Geology, 48*, 851–856.

Burkhard, M. (1990). Aspects of the large-scale Miocene deformation in the most external part of the Swiss Alps (sub-Alpine molasse to Jura fold belt). *Eclogae Geologicae Helvetiae, 83*(3), 559–583.

Chester, F. M., Rowe, C., Ujiie, K., Kirkpatrick, J., Regalla, C., Remitti, F., Moore, J. C., Toy, V., Wolfson-Schwehr, M., & Bose, S. (2013). Structure and composition of the plate-boundary slip zone for the 2011 Tohoku-Oki earthquake. *Science, 342*(6163), 1208–1211.

Decker, K., Schneeberger, R. & H. Madritsch. (2022). Paleo-strain reconstruction for central northern Switzerland from drill core mapping. 20th Swiss Geoscience Meeting, 18–20th Nov. 2022, Lausanne.

De Haller, A., Mazurek, M., Spangenberg, J., & Möri, A. (2014). SF (Self-sealing of faults and paleo-fluid flow): Synthesis report. Mont Terri Technical Report, TR 08-02, 63 pp. Federal Office of Topography (swisstopo), Wabern, Switzerland. www.mont-terri.ch

Dehandschutter, B., Vandycke, S., Sintubin, M., Vandenberghe, N., Gaviglio, P., Sizun, J.-P., & Wouters, L. (2004). Microfabric of fractured Boom Clay at depth: A case study of brittle–ductile transitional clay behaviour. *Applied Clay Science, 26*(1–4), 389–401.

Dèzes, P., Schmid, S., & Ziegler, P. (2004). Evolution of the European Cenozoic Rift System: Interaction of the Alpine and Pyrenean orogens with their foreland lithosphere. *Tectonophysics, 389*(1–2), 1–33.

Diehl, T., Madritsch, H., Schnellmann, M., Spillmann, T., Brockmann, E., & Wiemer, S. (2023). Seismotectonic evidence for present-day transtensional reactivation of the slowly deforming Hegau-Bodensee Graben in the northern foreland of the Central Alps. *Tectonophysics, 846*, 229659.

Dielforder, A., Berger, A., & Herwegh, M. (2016). The accretion of foreland basin sediments during early stages of continental collision in the European Alps and similarities to accretionary wedge tectonics. *Tectonics, 35*(10), 2216–2238.

Dielforder, A., Villa, I. M., Berger, A., & Herwegh, M. (2022). Tracing wedge-internal deformation by means of strontium isotope systematics of vein carbonates. *Geological Magazine*. https://doi.org/10.1017/S0016756821001357

Dielforder, A., Vollstaedt, H., Vennemann, T., Berger, A., & Herwegh, M. (2015). Linking megathrust earthquakes to brittle deformation in a fossil accretionary complex. *Nature Communications, 6*(1), 7504.

Ebert & Decker. (2019). Structural analysis manual. Nagra Arbeitsbericht. NAB 19-012, Wettingen, Switzerland.

Egli, D., Mosar, J., Ibele, T., & Madritsch, H. (2017). The role of precursory structures on Tertiary deformation in the Black Forest—Hegau region. *International Journal of Earth Sciences, 106*(7), 2297–2318.

Fernandez, A., Müller, I. A., Rodríguez-Sanz, L., van Dijk, J., Looser, N., & Bernasconi, S. M. (2017). A reassessment of the precision of carbonate clumped isotope measurements: Implications for calibrations and paleoclimate reconstructions. *Geochemistry, Geophysics, Geosystems, 18*(12), 4375–4386.

Ferrill, D. A., Morris, A. P., Hennings, P. H., & Haddad, D. E. (2014). Faulting and fracturing in shale and self-sourced reservoirs: Introduction. *AAPG Bulletin, 98*(11), 2161–2164.

Gautschi, A. (2017). Safety-relevant hydrogeological properties of the claystone barrier of a Swiss radioactive waste repository: An evaluation using multiple lines of evidence. *Grundwasser, 22*(3), 221–233.

Gimmi, T., Waber, H., Gautschi, A., & Rübel, A. (2007). Stable water isotopes in pore water of Jurassic argillaceous rocks as tracers for solute transport over large spatial and temporal scales. *Water Resources Research*. https://doi.org/10.1029/2005WR004774

Guglielmi, Y., Birkholzer, J., Rutqvist, J., Jeanne, P., & Nussbaum, C. (2017). Can fault leakage occur before or without reactivation? Results from an in situ fault reactivation experiment at Mont Terri. *Energy Procedia, 114*, 3167–3174.

Guglielmi, Y., Elsworth, D., Cappa, F., Henry, P., Gout, C., Dick, P., & Durand, J. (2015). In situ observations on the coupling between hydraulic diffusivity and displacements during fault reactivation in shales. *Journal of Geophysical Research: Solid Earth, 120*(11), 7729–7748.

Guillong, M., Wotzlaw, J.-F., Looser, N., & Laurent, O. (2020). Evaluating the reliability of U-Pb laser ablation inductively coupled plasma mass spectrometry (LA-ICP-MS) carbonate geochronology: Matrix issues and a potential calcite validation reference material. *Geochronology, 2*(1), 155–167.

Hancock, P. L. (1985). Brittle microtectonics: principles and practice. Journal of structural geology, 7(3-4);437–457.

Hergert, T., Heidbach, O., Reiter, K., Giger, S., & Marschall, P. (2015). Stress field sensitivity analysis in a sedimentary sequence of the Alpine foreland, northern Switzerland. *Solid Earth, 6*(2), 533–552.

Hinsken, S., Ustaszewski, K., & Wetzel, A. (2007). Graben width controlling syn-rift sedimentation: The Palaeogene southern Upper Rhine Graben as an example. *International Journal of Earth Sciences, 96*(6), 979–1002.

Hofmann, F., Schlatter, R., & Weh, M. (2000). Blatt 1011 Beggingen (Südhälfte) mit SW-Anteil von Blatt 1012 Singen. *Geol. Atlas Schweiz, 1*(25), 000.

Houben, M., Desbois, G., & Urai, J. (2013). Pore morphology and distribution in the Shaly facies of Opalinus Clay (Mont Terri, Switzerland): Insights from representative 2D BIB–SEM investigations on mm to nm scale. *Applied Clay Science, 71*, 82–97.

Houben, M., Desbois, G., & Urai, J. (2014). A comparative study of representative 2D microstructures in Shaly and Sandy facies of Opalinus Clay (Mont Terri, Switzerland) inferred form BIB-SEM and MIP methods. *Marine and Petroleum Geology, 49*, 143–161.

Housen, B. A., Tobin, H. J., Labaume, P., Leitch, E. C., & Maltman, A. J. (1996). Strain decoupling across the decollement of the Barbados accretionary prism. *Geology, 24*(2), 127–130.

Howard, D. L., de Jonge, M. D., Afshar, N., Ryan, C. G., Kirkham, R., Reinhardt, J., Kewish, C. M., McKinlay, J., Walsh, A., Divitcos, J., Basten, N., Adamson, L., Fiala, T., Sammut, L., & Paterson, D. J. (2020). The XFM beamline at the Australian Synchrotron. *Journal of Synchrotron Radiation, 27*, 1447–1458.

Ingram, G. M., & Urai, J. L. (1999). Top-seal leakage through faults and fractures: The role of mudrock properties. *Geological Society, London, Special Publications, 158*(1), 125–135.

Ishii, E. (2012). Microstructure and origin of faults in siliceous mudstone at the Horonobe Underground Research Laboratory site, Japan. *Journal of Structural Geology, 34*, 20–29.

Jaeggi, D., Laurich, B., Nussbaum, C., Schuster, K., & Connolly, P. (2018). Tectonic structure of the "main fault" in the Opalinus Clay, Mont Terri rock laboratory (Switzerland). Mont Terri Rock Laboratory, 20 Years: Two Decades of Research and Experimentation on Claystones for Geological Disposal of Radioactive Waste, 69–86.

John, C. M., & Bowen, D. (2016). Community software for challenging isotope analysis: First applications of 'Easotope'to clumped isotopes. *Rapid Communications in Mass Spectrometry, 30*(21), 2285–2300.
Jordan, P. (1992). Evidence for large-scale decoupling in the Triassic evaporites of Northern Switzerland: An overview. *Eclogae Geologicae Helvetiae, 85*(3), 677–693.
Jordan, P., Malz, A., Heuberger, S., Pietsch, J., Kley, J., & Madritsch, H. (2015). Regionale geologische Profilschnitte durch die Nordschweiz und 2D-Bilanzierung der Fernschubdeformation im östlichen Faltenjura: Arbeitsbericht zu SGT Etappe 2. Nagra Arbeitsbericht NAB, 14, 105, Nagra, Wettingen, Switzerland.
Keller, L. M., Schuetz, P., Erni, R., Rossell, M. D., Lucas, F., Gasser, P., & Holzer, L. (2013). Characterization of multi-scale microstructural features in Opalinus Clay. *Microporous and Mesoporous Materials, 170*, 83–94.
Kempf, O., & Pfiffner, O. A. (2004). Early Tertiary evolution of the North Alpine Foreland Basin of the Swiss Alps and adjoining areas. *Basin Research, 16*(4), 549–567.
Kim, S.-T., & O'Neil, J. R. (1997). Equilibrium and nonequilibrium oxygen isotope effects in synthetic carbonates. *Geochimica Et Cosmochimica Acta, 61*(16), 3461–3475.
Klinkenberg, M., Kaufhold, S., Dohrmann, R., & Siegesmund, S. (2009). Influence of carbonate microfabrics on thefailure strength of claystones. Engineering Geology, 107(1-2), 42–54.
Labaume, P., Maltman, A. J., Bolton, A., Tessier, D., Ogawa, Y., Takizawa, S., & Shipley, T. H. (1997). Scaly fabrics in sheared clays from the décollement zone of the Barbados accretionary prism. In Proceedings-Ocean Drilling Program Scientific Results (pp. 59–78). National Science Foundation.
Lanari, P., Vho, A., Bovay, T., Airaghi, L., & Centrella, S. (2019). Quantitative compositional mapping of mineral phases by electron probe microanalyser. *Geological Society, London, Special Publications, 478*(1), 39–63.
Lanari, P., Vidal, O., De Andrade, V., Dubacq, B., Lewin, E., Grosch, E. G., & Schwartz, S. (2014). XMapTools: A MATLAB©-based program for electron microprobe X-ray image processing and geothermobarometry. *Computers & Geosciences, 62*, 227–240.
Laubscher, H. (1961). Die fernschubhypothese der jurafaltung. *Eclogae Geologicae Helvetiae, 54*(1), 222–282.
Lauper, B., Zimmerli, G. N., Jaeggi, D., Deplazes, G., Wohlwend, S., Rempfer, J., & Foubert, A. (2021). Quantification of lithological heterogeneity within Opalinus Clay: Toward a uniform subfacies classification scheme using a novel automated core image recognition tool. *Frontiers in Earth Science, 9*, 645596.
Laurich, B., Urai, J. L., Desbois, G., Vollmer, C., & Nussbaum, C. (2014). Microstructural evolution of an incipient fault zone in Opalinus Clay: Insights from an optical and electron microscopic study of ion-beam polished samples from the Main Fault in the Mt-Terri Underground Research Laboratory. *Journal of Structural Geology, 67*, 107–128.
Laurich, B., Urai, J. L., & Nussbaum, C. (2017). Microstructures and deformation mechanisms in Opalinus Clay: Insights from scaly clay from the Main Fault in the Mont Terri Rock Laboratory (CH). *Solid Earth, 8*(1), 27–44.
Laurich, B., Urai, J. L., Vollmer, C., & Nussbaum, C. (2018). Deformation mechanisms and evolution of the microstructure of gouge in the Main Fault in Opalinus Clay in the Mont Terri rock laboratory (CH). *Solid Earth, 9*(1), 1–24.
Leflèvre, M., Guglielmi, Y., Henry, P., Dick, P., & Gout, C. (2016). Calcite veins as an indicator of fracture dilatancy and connectivity during strike-slip faulting in Toarcian shale (Tournemire tunnel, Southern France). *Journal of Structural Geology, 83*, 73–84.
Looser, N. S. H. (2022). Coupling clumped isotope thermometry and U-Pb dating of carbonates for applications in stratigraphy, diagenesis, and geodynamics (Doctoral dissertation, ETH Zurich).
Looser, N., Madritsch, H., Guillong, M., Laurent, O., Wohlwend, S., & Bernasconi, S. (2021). Absolute age and temperature constraints on deformation along the basal décollement of the Jura Fold-and-Thrust Belt from carbonate U-Pb dating and clumped isotopes. *Tectonics, 40*(3), e2020TC006439.
Madritsch, H. (2015). Outcrop-scale fracture systems in the Alpine foreland of central northern Switzerland: Kinematics and tectonic context. *Swiss Journal of Geosciences, 108*(2), 155–181.
Madritsch, H., Naef, H., Meier, B., Franzke, H. J., & Schreurs, G. (2018). Architecture and Kinematics of the Constance-Frick Trough (Northern Switzerland): Implications for the formation of Post-Variscan Basins in the Foreland of the Alps and scenarios of their neogene reactivation. *Tectonics, 37*(7), 2197–2220.
Malz, A., Madritsch, H., Jordan, P., Meier, B., & Kley, J. (2020). Along-strike variations in thin-skinned thrusting style controlled by pre-existing basement structure in the easternmost Jura Mountains (Northern Switzerland). *Geological Society, London, Special Publications, 490*(1), 199–220.
Malz, A., Madritsch, H., Meier, B., & Kley, J. (2016). An unusual triangle zone in the external northern Alpine foreland (Switzerland): Structural inheritance, kinematics and implications for the development of the adjacent Jura fold-and-thrust belt. *Tectonophysics, 670*, 127–143.
Mancktelow, N. S. (1993). Tectonic overpressure in competent mafic layers and the development of isolated eclogites. *Journal of Metamorphic Geology, 11*(6), 801–812.
Mancktelow, N. S. (2008). Tectonic pressure: Theoretical concepts and modelled examples. *Lithos, 103*(1–2), 149–177.
Mazurek, M. (2017). Gesteinsparameter-Datenbank Nordschweiz – Version 2. In: Nagra Arbeitsbericht NAB, vols.17–56. Wettingen, Switzerland.
Mazurek, M., & De Haller, A. (2018). Pore-water evolution and solute-transport mechanisms in Opalinus clay at Mont Terri and Mont Russelin (canton Jura, Switzerland). Mont Terri Rock Laboratory, 20 Years: Two Decades of Research and Experimentation on Claystones for Geological Disposal of Radioactive Waste, 131–151.
Mazurek, M., Alt-Epping, P., Bath, A., Gimmi, T., Waber, H. N., Buschaert, S., De Cannière, P., De Craen, M., Gautschi, A., & Savoye, S. (2011). Natural tracer profiles across argillaceous formations. *Applied Geochemistry, 26*(7), 1035–1064.
Mazurek, M., Davis, D. W., Madritsch, H., Rufer, D., Villa, I. M., Sutcliffe, C. N., De Haller, A., & Traber, D. (2018). Veins in clay-rich aquitards as records of deformation and fluid-flow events in northern Switzerland. *Applied Geochemistry, 95*, 57–70.
Mazurek, M., Hurford, A. J., & Leu, W. (2006). Unravelling the multi-stage burial history of the Swiss Molasse Basin: Integration of apatite fission track, vitrinite reflectance and biomarker isomerisation analysis. *Basin Research, 18*(1), 27–50.
Mazurek, M., & Aschwanden, L. (2020). Multi-scale petrographic and structural characterisation of the OpalinusClay. Nagra Arbeitsbericht, NAB, 19–44.
Meckler, A. N., Ziegler, M., Millán, M. I., Breitenbach, S. F., & Bernasconi, S. M. (2014). Long-term performance of the Kiel carbonate device with a new correction scheme for clumped isotope measurements. *Rapid Communications in Mass Spectrometry, 28*(15), 1705–1715.
Metz, B., Davidson, O., De Coninck, H., Loos, M., & Meyer, L. (2005). IPCC special report on carbon dioxide capture and storage. Cambridge: Cambridge University Press.
Müller, I. A., Fernandez, A., Radke, J., Van Dijk, J., Bowen, D., Schwieters, J., & Bernasconi, S. M. (2017). Carbonate clumped isotope analyses with the long-integration dual-inlet (LIDI) workflow: Scratching at the lower sample weight boundaries. *Rapid Communications in Mass Spectrometry, 31*(12), 1057–1066.
Muller, W., Aerden, D., & Halliday, A. N. (2000). Isotopic dating of strain fringe increments: Duration and rates of deformation in shear zones. *Science, 288*(5474), 2195–2198.
Nagra. (2014). SGT Etappe 2: Vorschlag Weiter zu Untersuchender Geologischer Standortgebiete Mit Zugehörigen Standortarealen für Die Oberflächenanlage. Geologische Grundlagen—Dossier II: Sedimentologische und Tektonische Verhältnisse Nagra Tech. Ber. NTB 14–02.
Nagra. (2021a). TBO Bülach 1-1: Data Report. Nagra Arbeitsbericht NAB 20-008, Nagra, Wettingen, Switzerland.
Nagra. (2021b). TBO Trüllikon 1-1: Data Report. Nagra Arbeitsbericht NAB 20-009, Nagra, Wettingen, Switzerland.
Nagra. (2021c). TBO Marthalen 1-1: Data Report. Nagra Arbeitsbericht NAB 21-020, Nagra, Wettingen, Switzerland.
Nagra. (2022a). TBO Bözberg 1-1: Data Report. Nagra Arbeitsbericht NAB 21-021, Wettingen, Nagra, Switzerland.
Nagra. (2022b). TBO Bözberg 2-1: Data Report. Nagra Arbeitsbericht NAB 21-022, Nagra, Wettingen, Switzerland.
Nagra. (2022c). TBO Stadel 3-1: Data Report. Nagra Arbeitsbericht NAB 22-001, Nagra, Wettingen, Switzerland.
Nagra. (2022d). TBO Stadel 2-1: Data Report. Nagra Arbeitsbericht NAB 22-002, Nagra, Wettingen, Switzerland.
Nagra. (2022e). TBO Bachs 1-1: Data Report. Nagra Arbeitsbericht NAB 22-004, Nagra, Wettingen, Switzerland.

Nagra. (2022f). TBO Rheinau 1-1: Data Report. Nagra Arbeitsbericht NAB 22-003, Nagra, Wettingen, Switzerland.
Nuriel, P., Wotzlaw, J.-F., Ovtcharova, M., Vaks, A., Stremtan, C., Šala, M., Roberts, N. M., & Kylander-Clark, A. R. (2021). The use of ASH-15 flowstone as a matrix-matched reference material for laser-ablation U— Pb geochronology of calcite. *Geochronology, 3*(1), 35–47.
Nussbaum, C., Kloppenburg, A., Caër, T., & Bossart, P. (2018). Tectonic evolution around the Mont Terri rock laboratory, northwestern Swiss Jura: constraints from kinematic forward modelling. Mont Terri Rock Laboratory, 20 Years: Two Decades of Research and Experimentation on Claystones for Geological Disposal of Radioactive Waste, 41–68.
Orellana, L. F., Nussbaum, C., Grafulha, L., Henry, P., & Violay, M. (2022). Physical characterization of fault rocks within the Opalinus Clay formation. *Scientific Reports, 12*(1), 1–13.
Paquette, J., & Reeder, R. J. (1995). Relationship between surface structure, growth mechanism, and trace element incorporation in calcite. *Geochimica Et Cosmochimica Acta, 59*(4), 735–749.
Passchier, C. W., & Trouw, R. A. (2005). *Microtectonics*. Springer Science & Business Media.
Peacock, D., & Sanderson, D. (1995). Pull-aparts, shear fractures and pressure solution. *Tectonophysics, 241*(1–2), 1–13.
Peacock, D. C. P., Nixon, C. W., Rotevatn, A., Sanderson, D. J., & Zuluaga, L. F. (2016). Glossary of fault and other fracture networks. Journal of Structural Geology, 92, 12–29.
Pfiffner, O. A. (1986). Evolution of the north Alpine foreland basin in the Central Alps. Foreland basins, 219–228.
Ramsay, J. G. (1980). The crack–seal mechanism of rock deformation. *Nature, 284*(5752), 135–139.
Ramsay, J. G., Huber, M. I., & Lisle, R. J. (1983). *The techniques of modern structural geology: Folds and fractures* (Vol. 2). Academic Press.
Reisdorf, A. G., & Wetzel, A. (2018). Evidence for synsedimentary differential tectonic movements in a low-subsidence setting: Early Jurassic in northwestern Switzerland. *Swiss Journal of Geosciences, 111*(3), 417–444.
Roberts, N. M., Rasbury, E. T., Parrish, R. R., Smith, C. J., Horstwood, M. S., & Condon, D. J. (2017). A calcitereference material for LA-ICP-MS U-Pb geochronology. Geochemistry, Geophysics, Geosystems, 18(7);2807–2814.
Roche, V., Childs, C., Madritsch, H., & Camanni, G. (2020). Layering and structural inheritance controls on fault zone structure in three dimensions: A case study from the northern Molasse Basin, Switzerland. *Journal of the Geological Society, 177*(3), 493–508.
Ryan, C. G., Etschmann, B. E., Vogt, S., Maser, J., Harland, C. L., van Achterbergh, E., & Legnini, D. (2005). Nuclear microprobe—Synchrotron synergy: Towards integrated quantitative real-time elemental imaging using PIXE and SXRF. *Nuclear Instruments and Methods in Physics Research B, 231*, 183–188.
Ryan, C. G., & Jamieson, D. N. (1993). Dynamic analysis: On-line quantitative PIXE microanalysis and its use in overlap-resolved elemental mapping. *Nuclear Instruments and Methods in Physics Research Section B: Beam Interactions with Materials and Atoms, 77*, 203–214.
Ryan, C., Kirkham, R., de Jonge, M., Siddons, D., Ent, A., Pagés, A., Bösenberg, U., Kuczewski, A., Dunn, P., Jensen, M., Liu, W., Harris, H., Moorhead, G., Paterson, D., Howard, D., Afshar, N., Garrevoet, J., Spiers, K., Falkenberg, G., & Pearce, M. (2018). The Maia Detector and Event Mode. *Synchrotron Radiation News, 31*, 21–27.
Schmid, S. M., Pfiffner, O.-A., Froitzheim, N., Schönborn, G., & Kissling, E. (1996). Geophysical-geological transect and tectonic evolution of the Swiss-Italian Alps. *Tectonics, 15*(5), 1036–1064.
Schori, M., Mosar, J., & Schreurs, G. (2015). Multiple detachments during thin-skinned deformation of the Swiss Central Jura: A kinematic model across the Chasseral. *Swiss Journal of Geosciences, 108*(2), 327–343.
Schrank, C. E., Jones, M. W. M., Kewish, C. M., van Riessen, G. A., Elphick, K. E., Nothdurft, L. D., Webb, G. E., Paterson, D. J., & Regenauer-Lieb, K. (2021). Micro-scale dissolution seams mobilise carbon in deep sea limestones. *Communications Earth & Environment, 2*, 174.
Schreiner, A. (1992). Geological Map of Baden-Württemberg 1:50000: Hegau und westlicher Bodensee. Annotations. LGRB, Freiburg, 290 pp.
Sibson, R. H. (1981). Controls on low-stress hydro-fracture dilatancy in thrust, wrench and normal fault terrains. *Nature, 289*(5799), 665–667.
Siegesmund, S., Popp, T., Kaufhold, A., Dohrmann, R., Gräsle, W., Hinkes, R., & Schulte-Kortnack, D. (2014). Seismic and mechanical properties of Opalinus Clay: comparison between sandy and shaly facies from Mont Terri (Switzerland). Environmental earth sciences, 71, 3737–3749.
Siddons, D. P., Kirkham, R., Ryan, C. G., De Geronimo, G., Dragone, A., Kuczewski, A. J., Li, Z. Y., Carini, G. A., Pineli, D., Beuttenmuller, R., Elliot, D., Pfeffer, M., Tyson, T. A., Moorhead, G. F., & Dunn, P. A. (2014). Maia X-ray microprobe detector array system. *Journal of Physics: Conference Series, 499*, 012001.
Sinclair, H., & Allen, P. (1992). Vertical versus horizontal motions in the Alpine orogenic wedge: Stratigraphic response in the foreland basin. *Basin Research, 4*(3–4), 215–232.
Smeraglia, L., Fabbri, O., Choulet, F., Buatier, M., Boulvais, P., Bernasconi, S. M., & Castorina, F. (2020). Syntectonic fluid flow and deformation mechanisms within the frontal thrust of a foreland fold-and-thrust belt: Example from the Internal Jura, Eastern France. *Tectonophysics, 778*, 228178.
Smeraglia, L., Fabbri, O., Choulet, F., Jaggi, M., & Bernasconi, S. M. (2022). The role of thrust and strike-slip faults in controlling regional-scale paleofluid circulation in fold-and-thrust belts: Insights from the Jura Mountains (eastern France). *Tectonophysics, 829*, 229299.
Smeraglia, L., Looser, N., Fabbri, O., Choulet, F., Guillong, M., & Bernasconi, S. M. (2021). U-Pb dating of middle Eocene-middle Pleistocene multiple tectonic pulses in the Alpine foreland. *Solid Earth Discussions, 2021*, 1–14.
Sommaruga, A. (1999). Décollement tectonics in the Jura forelandfold-and-thrust belt. *Marine and Petroleum Geology, 16*(2), 111–134.
Sommaruga, A., Mosar, J., Schori, M., & Gruber, M. (2017). The role of the Triassic evaporites underneath the North Alpine Foreland. In Permo-Triassic Salt Provinces of Europe, North Africa and the Atlantic Margins (pp. 447–466). Elsevier.
Song, J., & Zhang, D. (2013). Comprehensive review of caprock-sealing mechanisms for geologic carbon sequestration. *Environmental Science & Technology, 47*(1), 9–22.
Teng, H. H., Dove, P. M., & De Yoreo, J. J. (2000). Kinetics of calcite growth: Surface processes and relationships to macroscopic rate laws. *Geochimica Et Cosmochimica Acta, 64*, 2255–2266.
Vermeesch, P. (2018). IsoplotR: A free and open toolbox for geochronology. *Geoscience Frontiers, 9*(5), 1479–1493.
Vernon, R. H. (2004). *A practical guide to rock microstructure*. University Press Cambridge.
Wenning, Q. C., Madonna, C., Zappone, A., Grab, M., Rinaldi, A. P., Plötze, M., Nussbaum, C., Giardini, D., & Wiemer, S. (2021). Shale fault zone structure and stress dependent anisotropic permeability and seismic velocity properties (Opalinus Clay, Switzerland). *Journal of Structural Geology, 144*, 104273.
Wersin, P., Gimmi, T., Mazurek, M., Alt-Epping, P., Pękala, M., & Traber, D. (2018). Multicomponent diffusion in a 280 m thick argillaceous rock sequence. *Applied Geochemistry, 95*, 110–123.
Wersin, P., Mazurek, M., Mäder, U. K., Gimmi, T., Rufer, D., Lerouge, C., & Traber, D. (2016). Constraining porewater chemistry in a 250 m thick argillaceous rock sequence. *Chemical Geology, 434*, 43–61.
Wetzel, A., Allenbach, R., & Allia, V. (2003). Reactivated basement structures affecting the sedimentary facies in a tectonically "quiescent" epicontinental basin: An example from NW Switzerland. *Sedimentary Geology, 157*(1–2), 153–172.
Willett, S. D., & Schlunegger, F. (2010). The last phase of deposition in the Swiss Molasse Basin: From foredeep to negative-alpha basin. *Basin Research, 22*(5), 623–639.
Winhausen, L., Khaledi, K., Jalali, M., Urai, J. L., & Amann, F. (2022). Failure mode transition in Opalinus Clay: A hydro-mechanical and microstructural perspective. *Solid Earth, 13*(5), 901–915.
Winhausen, L., Klaver, J., Schmatz, J., Desbois, G., Urai, J. L., Amann, F., & Nussbaum, C. (2021). Micromechanisms leading to shear failure of Opalinus Clay in a triaxial test: A high-resolution BIB–SEM study. *Solid Earth, 12*(9), 2109–2126.
Ziegler, P. A. (1990). Geological atlas of western and central Europe, 239. Mijdrecht: Shell International Petroleum.

Publisher's Note